

Bifunctional Europium Oxide Chloride in the Methane Oxychlorination Reaction: Catalyst and Thermometer

On finding boundary conditions for reliable temperature measurements using band shape thermometry during the methane oxychlorination reaction

Tjom Arens

Supervisors:
Bas Terlingen
dr. Freddy Rabouw
prof. dr. ir. Bert Weckhuysen



Universiteit Utrecht

Inorganic Chemistry & Catalysis
Utrecht University
September 20, 2021

Table of Contents

ABSTRACT	3
1 INTRODUCTION	4
2 THEORY	6
2.1 Luminescence thermometry.....	6
2.2 Nanothermometer performances	8
2.3 Luminescence lifetimes	9
3 EXPERIMENTAL METHODS	13
3.1 Catalyst synthesis.....	13
3.2 Catalyst characterization	13
3.3 Catalytic testing	13
4 RESULTS AND DISCUSSION	14
4.1 Catalyst characterization	14
4.2 EuOCl as thermometer in inert environment	14
4.3 Applicability of EuOCl as thermometer under MOC reaction conditions	17
4.3.1 Homogenous catalyst chlorination.....	18
4.3.2 The thermal quenching of the luminescence signal	20
4.3.3 The effect of catalyst chlorination on the I^{5D_1}/I^{5D_0} ratio and on the luminescence emission spectrum of europium.....	24
4.4 Temperature measurements during the methane oxychlorination reaction.....	29
5 CONCLUSION	36
6 OUTLOOK	37
ACKNOWLEDGMENT	37
LITERATURE LIST:	38
SUPPORTING INFORMATION:	42

ABSTRACT

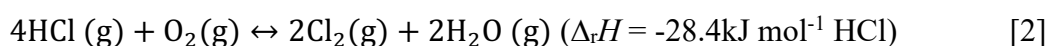
The abundance of methane has made its direct conversion to chemicals one of the main topics in hydrocarbon research for several decades. A promising route for the direct conversion of methane is via the methane oxychlorination (MOC) reaction over EuOCl. This reaction offers good catalytic performances with high chloromethane selectivities ($> 50\%$) and methane conversion levels ($> 30\%$) at moderate reaction temperatures ($\sim 425\text{ }^{\circ}\text{C}$). The MOC reaction is exothermic and therefore the local temperature of the catalyst can deviate from the set temperature. Monitoring the temperature is important for investigation of the thermodynamics and kinetics of the reaction, stability of the catalyst, and early detection of thermal runaway. In this thesis we use luminescence band shape thermometry to determine the local temperature of our EuOCl catalyst during the MOC reaction. Luminescence band shape thermometry is a non-invasive, cheap, and practical technique with high thermal stability and therefore ideal for temperature monitoring during the MOC reaction. In an inert environment, temperature determination with the ${}^5\text{D}_1/{}^5\text{D}_0$ luminescence intensity ratio of europium was accurate. The ${}^5\text{D}_1/{}^5\text{D}_0$ luminescence intensity ratio was however not only temperature dependent, but also changed drastically and irreversibly upon bulk chlorination of EuOCl under MOC reaction conditions. At reaction temperatures of $\geq 475\text{ }^{\circ}\text{C}$ bulk chlorination was significantly reduced, and the local temperature was accurately determined. The temperature increase observed during the MOC reaction scaled proportionally with the reaction gas concentrations. The maximum temperature increase was $\sim +6\text{ }^{\circ}\text{C}$ and temperature changes were reproducible. Under isothermal conditions ($475\text{ }^{\circ}\text{C}$), dilution of the gas feed with helium ($\sim 110\text{ }^{\circ}\text{C}$) resulted in cooling of the catalyst bodies and no signs of thermal runaway were observed during MOC. The method used for luminescence thermometry enables local temperature determination in the absence of dopant thermometer particles. Additionally, temperature determination in closer proximity to the active site of the catalyst could be possible compared to the use of dopant thermometer particles. Investigation of the bifunctional use of other lanthanide-based catalyst can be interesting when temperature effects can be separated from other effects. This could increase the accuracy of temperature measurements, while reducing the costs.

1 INTRODUCTION

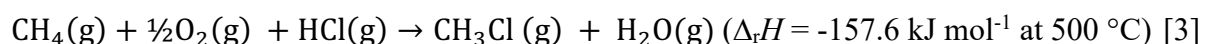
The activation of methane plays a key role in securing the supply of energy, chemicals and fuels in the future.^{1,2} Methane is the principal component of natural gas and biogas. Furthermore, it can be found in crystalline hydrates located in many oceans and permafrost areas.² This abundance of methane has made its conversion to chemicals one of the main topics in hydrocarbon research for several decades.¹ However, selective activation of the inert C-H bonds in alkanes, and especially methane, is difficult due to their high chemical stability.³ The high chemical stability of methane and other alkanes can be explained according to their electronic structure. Alkanes have an equal number of valence electrons; lone pairs and empty orbitals are absent. On top of that, the low polarity, high binding energy of the C-H bond (100 kcal/mol) and steric hindrance of the tetrahedral arrangement result in low reactivity.⁴ The use of an electrophilic halogen or halogen compound for methane activation results in the formation of halogenated methyl products.^{2,3} Although methane can react with all halogens forming halogenated products, only the reaction with chlorine and bromine are of practical interest for large-scale processes. Especially the production of chloromethane is of great interest due to its chemical analogy with methanol.^{2,5} Currently, chloromethane is produced on a large-scale via the thermal chlorination of methane using chlorine gas (eq. 1).^{2,3}



During this radical gas-phase reaction with Cl_2 , HCl is formed as a byproduct. Although, the field of application of HCl is extremely wide, supply and demand are not balanced.⁶⁻¹¹ Especially the fast growing demand for polyurethanes and polycarbonates has resulted in additional formation of HCl as by-product.¹² Comparison of production and demand for HCl shows that about 15% of the by-product HCl is used in production, 45% is sold to consumers, and 30% has no sales.¹³ Disposal of this 30% is costly and therefore alternative sustainable routes for the use of HCl are needed.¹² A possible route, which has been under investigation for two centuries, is the gas phase oxidation of HCl with air or oxygen first established by Henry Deacon in 1870.¹² The so-called Deacon reaction is an attractive route for the chlorine recovery due to its low electrical power and thermal requirements and its relative ease of application. The Deacon process is reversible, exothermic and proceeds via (eq. 2):¹⁴

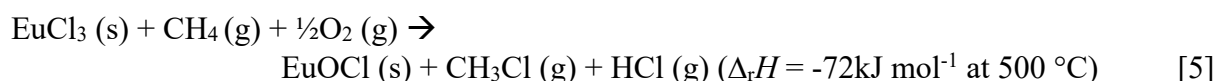
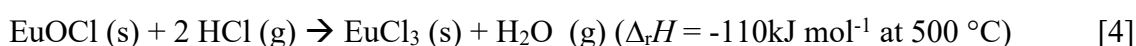


A newer promising route for the use of by product HCl is the direct production of chloromethanes from methane via the Methane Oxychlorination (MOC) reaction.¹⁵⁻²⁰



The selectivity to methyl chloride (CH_3Cl) is usually low as the incorporation of each successive chlorine increases the reactivity of the product.²¹ The MOC reaction however offers a relatively high selectivity to the desired product, while being performed under moderate reaction conditions (1 bar, < 500 °C) in the presence of a catalyst.¹ A challenge lies at higher conversion rates as the formation of CO and CO_2 via the destructive adsorption of $\text{CH}_x\text{Cl}_{4-x}$ and the formation of CO_2 due to methane combustion pose a problem for the selectivity of the reaction.^{3,5,22} Lercher et al.³ were the first to report on a lanthanide-based catalyst for the MOC reaction forming CH_3Cl . Using a LaCl_3 -based catalyst and high CH_4 concentrations, to limit conversion, a high selectivity (73%) towards CH_3Cl was achieved, while limiting the CH_2Cl_2 selectivity (18%). However, only at low conversion levels (<10%) these high selectivities could be obtained. Recent work by Terlingen et al.⁵ has shown that lanthanide (III) oxide chloride

catalysts have great potential for the MOC reaction. EuOCl is the most promising of those catalyst as very high conversion levels (> 30%) and high selectivity towards chloromethane (> 50%) can be reached at moderate reaction temperatures (~425 °C). *Operando* Raman spectroscopy revealed that the chlorination of the catalyst was the rate limiting step over EuOCl. Therefore, increasing HCl concentration from 10% to 60% at 450 °C resulted in a drastic decrease in CO selectivity (30% to 15%) and an increase in CH₄ conversion (11% to 24%). Apart from the HCl concentration, the activity is also strongly dependent on the temperature. At 80% HCl concentration a maximum conversion of 42% could be reached at 505 °C. The oxychlorination cycle over EuOCl is expected to be similar to that over LaOCl and thus consists of 3 key reaction steps: (I) chlorination of the catalyst (eq. 4), (II) activation of Cl by dissociative addition of oxygen and (III) chlorination of methane, also-called dechlorination of the catalyst (eq. 5).^{3,21} Figure 1 shows the MOC reaction mechanism over EuOCl.



The chlorination and dechlorination of EuOCl are both exothermic reactions and therefore the local temperature of the catalyst (T_{local}) is expected to be higher than the set temperature (T_{set}) (Fig. 1). This temperature difference can affect the kinetics, thermodynamics, and stability of the catalyst.

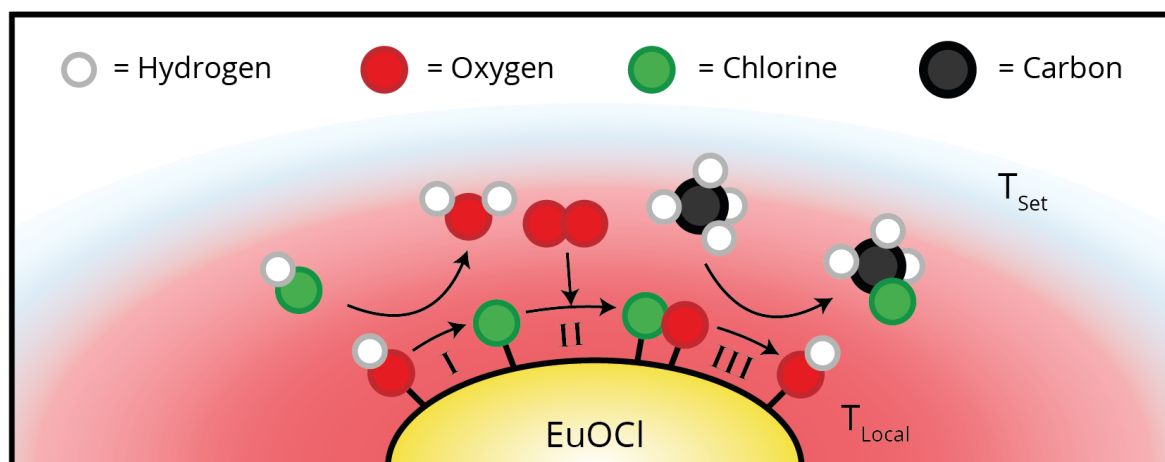


Figure 1. MOC cycle over EuOCl consisting of 3 steps: (I) chlorination of the catalyst, (II) activation of chlorine by oxygen and (III) chlorination of methane (dechlorination of the catalyst). Chlorination and dechlorination of the catalyst are exothermic the local temperature (T_{local}) can therefore be higher compared to the set temperature of the oven (T_{set}).

When operating an exothermic reaction, the risk of thermal runaway is always present and causes both safety and economic risk. Therefore, constant monitoring of the temperature is required. Thermal runaway begins when the produced heat exceeds the removed heat. Due to the rising temperature the activity of the reaction increases causing even more surplus heat, which can eventually lead to loss of control over the reaction.^{23,24} Temperature monitoring is not only required for safety concerns, but also important for optimization of a reaction. When temperature is heterogeneously distributed through a reactor, reactions conditions can differ from optimal conditions reducing catalyst performances.²⁵

An ideal thermometer for the monitoring of temperature during a reaction should be non-invasive, have a high thermal stability and should function in a cheap and practical manner.²⁶

A technique that ticks all those boxes is luminescence thermometry.²⁷ Luminescence thermometry uses a certain temperature dependent luminescence parameter (spectral position^{28,29}, band shape^{25,30,31}, band width^{32,33}, peak intensity³⁴, polarization or lifetimes^{30,32}) to determine and monitor the temperature of the catalyst. In this study, we focus on band shape thermometry, the intensity ratio between two peaks, to monitor the local temperature of our EuOCl catalyst during the MOC reaction. The luminescent Eu³⁺ center functions both as a catalyst and as a thermometer. This is different from the common method for nano thermometry where the catalyst is doped with thermometer particles. The absence of additional thermometer dopants reduces the distance between the thermometer particle and active site. Therefore, the temperature of the active catalyst can be monitored more locally and in the absence of dopants. In this new method, the thermometer particles are not inert during the MOC reaction and therefore the effect of MOC reaction conditions on the reliability of the thermometer is important. This study first shows the viability of EuOCl as a thermometer under inert conditions. Then, the reaction condition boundaries for reliable temperature measurements during the MOC reaction are described, especially the limitation of bulk chlorination is important. Finally, the established boundaries for reliable temperature measurements during the MOC reaction are applied to study the effect of the reaction gas mixture on the formed reaction heat and to study the reproducibility of the temperature measurements.

2 THEORY

2.1 Luminescence thermometry

The word luminescence is based on the latin word lumen, which means light, and was first used in 1888 by the German physicist, Eilhardt Wiedemann.^{35,36} In luminescence, electrons are excited from the ground state to an excited state by some external excitation source. Hereafter, photons are emitted, with an energy equal to the gap between the two states, upon falling back to the ground state.³⁶ The properties of the emitted photons depend on the properties of those energy states involved in the emissions. Therefore, measuring the emission of emitted photons can give information about the emitter.²⁷ Lanthanide-based materials are well-known luminescent materials because of the interesting photoluminescent properties lanthanide ions have to offer. The lanthanide series is characterized by the partially filled 4f orbitals of its trivalent ions, [Xe]5s²5p⁶4f⁰ (for La³⁺) to 4f¹⁴ (for Lu³⁺). Upon irradiation with UV, several of these lanthanides emit in the visible or near-infrared spectral regions. The color of the emitted light depends on the respective lanthanide ion.³⁷ The 4f-orbitals of these lanthanides are shielded by the more outlying filled 5s and 5p orbitals. Electrons in the 4f-orbitals do therefore not participate in chemical bonding and emission from these levels are relatively insensitive to the chemical environment. The emission spectra of lanthanides are characterized by sharp peaks and emissions are very similar in different environments.

The origin of these emission spectra is found in the energy levels of the electron configuration of these lanthanides (Fig. 2). These, in turn, are dependent on the kinetic energy of the electrons, the interaction between the 4f-electrons, core electrons and the nucleus.^{26,38} The total coulombic energy is dependent on the distribution of electrons over the different orbitals. A different distribution of electrons over the orbitals results in a different coulombic energy and therefore the energy levels are split into a multitude of different energy levels. Additionally, the energy levels are further split due to spin-orbit interaction, which accounts for the coupling of the spin angular momentum and the orbital angular momentum.³⁸ This phenomenon describes the electromagnetic interaction between the electron's magnetic dipole, orbital motion and the electrostatic field of the positively charged nucleus.³⁹ The splitting of energy levels and the insensitive nature of the lanthanides, due to 4f shielding, result in characteristic energy levels for each of the lanthanides. The energy level diagrams of all these trivalent

lanthanide ions combined was published in 1968 by Dieke et al.⁴⁰ and is referred to as a ‘Dieke diagram’. The energy levels of interest for europium in this study are shown in figure 2. Transitions between energy levels are possible through the absorption or emission of a photon. As these transitions between energy levels in a lanthanide are characteristic for that lanthanide so is the luminescence spectrum.

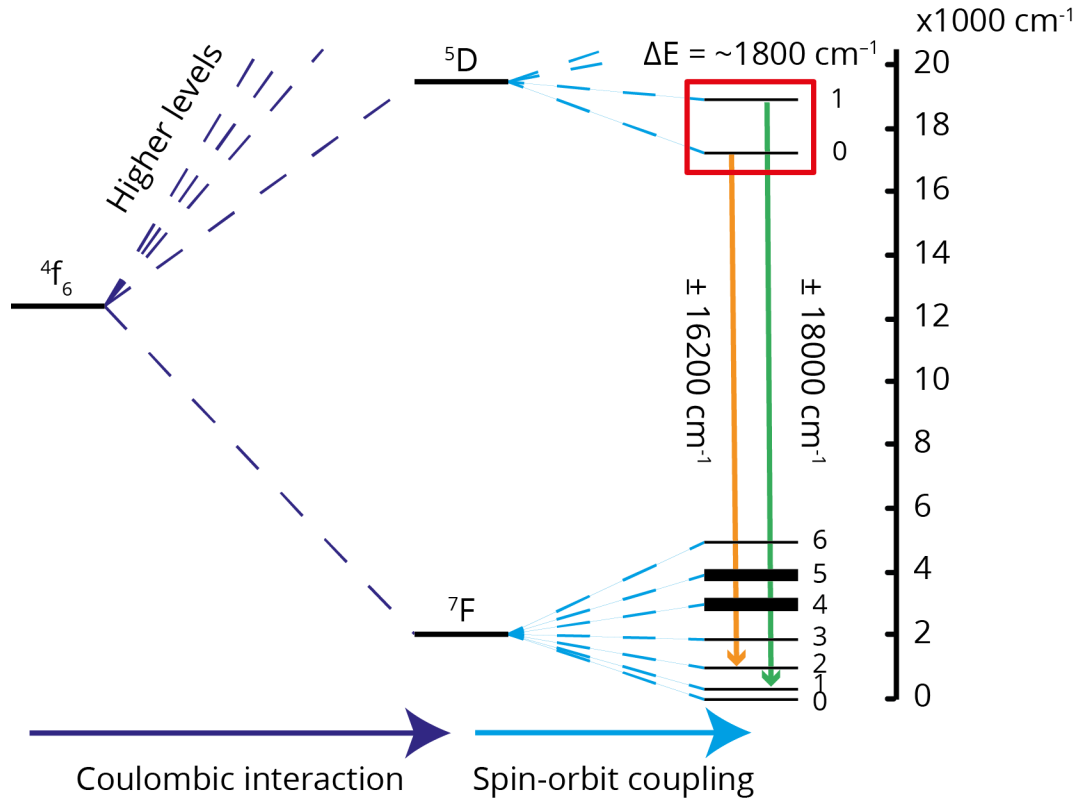


Figure 2. The energy level splitting of the 4f orbitals of europium due to coulombic interaction and spin-orbit coupling. The two thermally coupled states of europium, 5D_1 and 5D_0 , are shown with the important transitions from these levels.

A number of these lanthanides have energy levels that are so close together that thermal energy is sufficient for fast relaxation between the two states ($\Delta E < 2000 \text{ cm}^{-1}$), so-called thermally coupled states.⁴¹ In the case of europium, these states are the 5D_1 and 5D_0 excited states (Fig. 2, red box). The population distribution between the two states is strongly temperature dependent. When the lower energy excited state (5D_0) is populated due to an optical excitation from the ground state, this population is thermally redistributed to a slightly higher energy excited state (5D_1).²⁷ Note that in reality the 5D_1 level is triple degenerate, in this case however a simple 2 level system is assumed. The population in the higher-energy state, in a steady state condition, is given by (eq. 6):²⁷

$$N_{5D1} = N_{5D0} e^{-\frac{\Delta E}{k_B T}} \quad [6]$$

With N_{5D0} the population of the 5D_0 level, ΔE the energy difference between the two coupled states, 5D_0 and 5D_1 , k_B the Boltzmann constant and T the temperature. Since the emission intensity from an energy level is proportional to the population in the respective level, both energy levels, contribute to the luminescence spectrum. The intensity of the corresponding de-excitation, also called emission, from the excited level to the ground state, I_i , is given by (eq. 7):²⁷

$$I_i = \varphi_i N_i \quad [7]$$

With φ a constant with a value depending on geometrical factors as well as on intrinsic properties of the emitting state. Combining equation 6 and 7 and rewriting, gives the Boltzmann equation (eq. 8):²⁷

$$\frac{I_{5D1}}{I_{5D0}} = \frac{\varphi_{5D1} N_{5D1}}{\varphi_{5D0} N_{5D0}} = \frac{\varphi_{5D1}}{\varphi_{5D0}} e^{-\frac{\Delta E}{k_B T}} \quad [8]$$

Replacing the constant term $\frac{\varphi_{5D1}}{\varphi_{5D0}}$ with C we get the following relationship between temperature, ΔE and the intensity ratio of the two thermally coupled states (eq. 9):

$$\frac{I_{5D1}}{I_{5D0}} = C e^{-\frac{\Delta E}{k_B T}} \quad [9]$$

Thus, by experimental determination of the emissions from the two thermally coupled states the temperature can be calculated. However, note that to reach Boltzmann equilibrium, thermal energy should be sufficient to excite electrons over the energy difference ΔE and thus if ΔE becomes too large or T too small, temperature determination is impossible as the population in excited state 5D_1 is near zero and the signal will be overshadowed by noise.²⁶ On the other hand, when ΔE is too small or T too large the thermal population in N_{5D1} is so high that it is relatively unaffected by a change in T .⁴² Therefore, nano thermometers based on different lanthanides, with different ΔE , have different temperature ranges in which they can be used. At the top of the range measurements are precise but insensitive, while at the bottom of the range measurements are sensitive but noisy.⁴²

Another possible thermometry technique is spectral luminescence thermometry. This is based on the analysis of the peak position of the emission lines. These spectral positions are dependent on the energy separation between the two energy levels participating in the transition, which in turn depend on a variety of different, temperature dependent, parameters of the emitting material, including the refractive index and density of the material.²⁷ As the spectral position is dependent on temperature dependent parameters it will be temperature dependent itself. Therefore, these shifts in spectral position due to changes in the temperature can be exploited to determine the temperature of the material.²⁷ The shift in thermal position is dependent on the used material. Some materials will have a positive correlation between the spectral position and the temperature, while other materials have a negative correlation. Dai et al.²⁸ showed that, not only the material, but also the particle size can result in an opposite correlation. PbSe nanocrystals quantum dots with 3.9 nm particle size had a positive correlation, while the same particles with a size of 6.9 nm showed a negative correlation. Kolesnikov et al.²⁹ also found uses for spectral luminescence thermometry using the rare earth metal Erbium in $YVO_4:Er^{3+}$.

2.2 Nanothermometer performances

To describe the performances of a thermometer, two important parameters can be used, namely the accuracy and sensitivity of the thermometer. The accuracy of a thermometer gives the deviation between the true and the measured temperature, while the sensitivity describes how strongly the temperature dependent parameter reacts to a change in temperature.⁴³ The absolute thermal sensitivity describes the absolute change in the temperature dependent parameter for a variation in temperature and is given by (eq. 10):

$$S_a = \frac{dA}{dT} \quad [10]$$

Where A is the temperature dependent parameter. A can change significantly based on the chosen calculation procedure and therefore it is not a good measure to compare different thermometers.²⁹ A measure that can be used to compare the sensitivity of different thermometers is the relative sensitivity, S_r (eq. 11):

$$S_r = \frac{1}{A} \frac{dA}{dT} \quad [11]$$

In the case of a Boltzmann thermometer, based on the luminescence intensity ratio between two thermally coupled states, equation 11 can be rewritten to (eq. 12):

$$S_r = \frac{\Delta E}{k_B T^2} \quad [12]$$

The relative sensitivity of a Boltzmann thermometer shows the percentage change in the peak intensity ratio for a 1K change in temperature at a particular temperature. It is completely dependent on the ΔE value and thus depends on the used lanthanide ion.

The accuracy, or in other words the uncertainty in the measured temperature, of a thermometer is highly dependent on the noise in the measurement. In the case of band shape nano thermometry, the temperature is calculated by division of two peak areas, A and B. Both peaks are subject to shot noise, or the so-called Poisson error, and therefore, so is the calculated temperature. One of the two peaks will often be much smaller than the other and therefore will have a much bigger impact on the uncertainty in the temperature (eq. 13):⁴²

$$\sigma_T = \frac{k_B T^2}{\Delta E} \sqrt{\frac{1}{A} + \frac{1}{B}} \quad [13]$$

The temperature uncertainty is related to the temperature, ΔE value and the intensity of the peaks used for temperature determination. The temperature uncertainty can thus be minimized by increasing the number of counts, this is possible due to increasing the integration time, emission efficiency or the dopant concentration.⁴²

2.3 Luminescence lifetimes

To understand the effect of temperature on the luminescence of lanthanides it is important to know the processes that occur during excitation and emission of the electronic states of the lanthanide.⁴³ Electrons excited to an excited state decay at a rate (k), which is a combination of radiative (k_R) and non-radiative (k_{NR}) decay processes (eq. 14):

$$k = k_R + k_{NR} \quad [14]$$

The inverse of this decay rate is the time constant τ , also called the lifetime of the excited state (eq. 15):

$$\tau = \frac{1}{k_R + k_{NR}} \quad [15]$$

Radiative processes occur due to the emission of a photon, while non-radiative processes occur through the conversion to and loss of vibrational energy.⁴³ This loss in luminescence intensity due to non-radiative decay can occur through several processes, which are called ‘quenching’ processes. When the cause of quenching is a change in the temperature of the material it is

called temperature quenching. Temperature quenching forms the basis of all sorts of nano thermometry measurements. As radiative decay is temperature independent, while non-radiative decay is not, the latter can be used to describe the temperature effect on the luminescence intensity.⁴³

A common method to describe the effect of temperature on the non-radiative decay rate is through the Mott-Seitz theory, which is based on a simple configuration coordinate model consisting of parabolas shifting with respect to each other (Fig. 3).⁴⁴ These parabolas each represent the total energy of the system in either the ground or an excited state as a function of the configuration coordinate r .⁴³

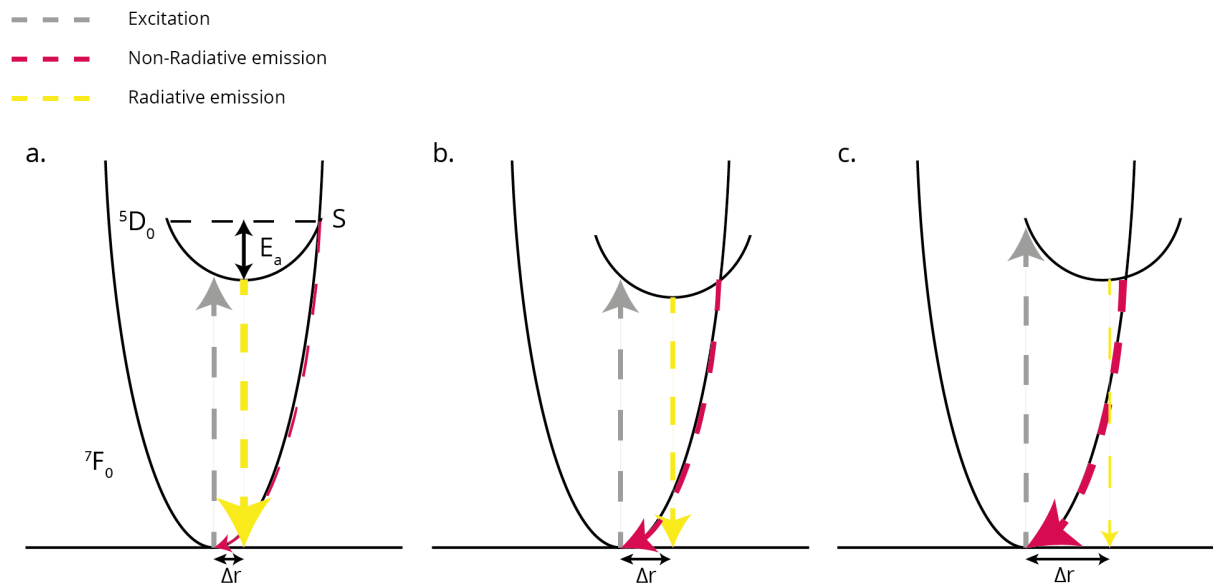


Figure 3. Configurative coordinate model. (a) Small Δr results in a high activation energy (E_a) and thus an efficient emitter. (b) Higher Δr results in a smaller E_a and thus more non-radiative decay (c) Δr is so large that all decay is non-radiative.

When an electron is excited from the ground state to the excited state (gray arrow) it can de-excite through the radiative (yellow arrow) or the non-radiative (red arrow) pathway depending on the orientation and temperature of the system. When thermal energy is sufficient to excite an electron over the activation energy, E_a , the electron can non-radiatively de-excite to the ground state through the intersection of the parabolas S with the rate (eq. 16):

$$k_{NR}(T) = A * e^{-\frac{E_a}{k_B T}} \quad [16]$$

The non-radiative decay rate increases with a smaller E_a or when the temperature decreases. Therefore, to achieve efficient luminescence and limit non-radiative decay at higher temperatures, the emission center should have a configuration coordinate curve of the excited state that lies within that of the ground state and thus a small Δr (Fig. 3b). Upon increasing the absolute Δr of the emission center it becomes easier to reach S and thus non-radiative decay increases compared to radiative decay. When the excited-state parabola lies outside of the ground state parabola all radiation is expected to be non-radiative (Fig. 3c).⁴⁵

Assuming that the curves of the excited state have a fixed shape and r , this model also describes the different quenching rates of the different energy levels of the excited states (Fig. 4). When the excited state moves to higher energies the activation energy needed to reach the intersection S goes up and temperature quenching decreases.

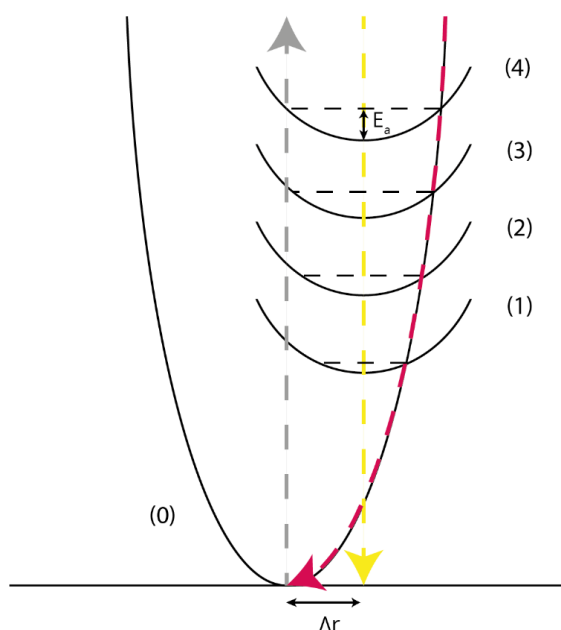


Figure 4. Configurational coordinate model with relatively big Δr showing that higher excited states have a bigger E_a and thus quench relatively slower compared to lower lying excited states.

Although, this theory explains the quenching of broadband emissions with a large Δr particularly well, it is less suitable for the narrow line f-emissions visible for the lanthanide series with $\Delta r =$ almost 0.⁴³ According to this model, the intersection between the excited and ground state for the lanthanides would be at very high energies and therefore temperature quenching would be expected to be small. However, quenching for the lanthanide series at higher temperatures is clearly visible.⁴⁶ Additionally, quenching of the higher energy excited states increases going to higher energies. This is opposite to the Mott-Seitz theory and thus another explanation is needed.

One explanation could be through phonon emission to the lattice mode, called multiphonon relaxation (Fig. 5a).⁴³ By the emission of multiple phonons with an energy $h\nu$, the energy-gap can be bridged non-radiatively. The rate of multiphonon emission decreases with the number of phonons needed to bridge the gap and it is believed that multiphonon relaxation with more than seven phonons are fairly probable.^{43,47} The maximum phonon energy is dependent on the host lattice and can be determined by investigation of the highest peak in the Raman spectrum. In the case of europium oxide chloride and europium chloride, the maximum phonon energy is expected to be $500 - 600 \text{ cm}^{-1}$ and $200 - 300 \text{ cm}^{-1}$ respectively,⁴⁸ the energy-gap between the 5D_1 and 5D_0 energy level of 1780 cm^{-1} can therefore be bridged due to multiphonon relaxation (Fig. 5a).⁴⁹ However, multiphonon relaxation over the energy gap between the lowest lying excited state and highest ground state in europium ($^5D_0 \rightarrow ^7F_6$) of approximately 12000 cm^{-1} is very improbable as it would require at least 20 phonons.⁴⁷ Non-radiative decay due to multiphonon relaxation in europium crystals with low impurity concentrations is thus low. However, if europium is incorporated in another crystal as a dopant or when impurity concentrations are high, the lattice can have energy levels in between the 5D_0 and 7F_6 state. This can reduce the number of phonons needed to bridge the gap and thereby increase the probability of the non-radiative transition and quench radiative emission (Fig. 5a).

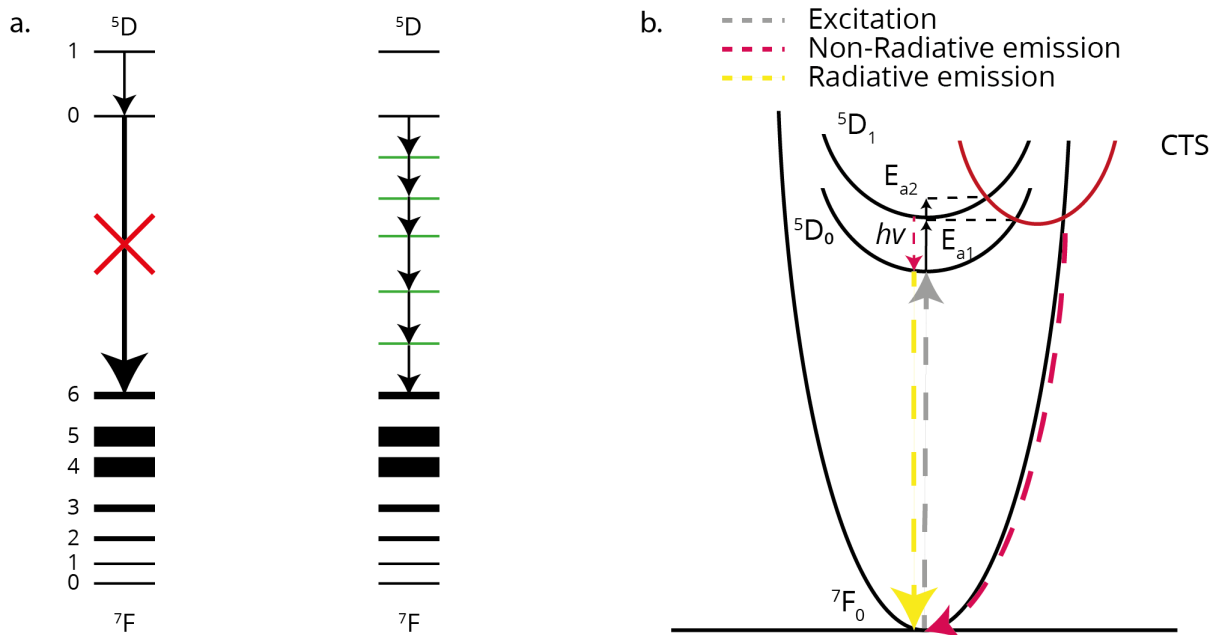


Figure 5. (a) Energy level diagrams of EuOCl with (left) or without (right) energy levels in between 5D_0 and 7F_6 levels due to impurities or host material. Multiphonon relaxation is improbable for pure EuOCl but is possible for doped europium or with high impurity concentrations. (b) Configurage coordinate model for Lanthanide ($\Delta r = 0$), charge transfer state quenches radiative decay through thermal assisted non-radiative decay via the intersection with the CTS to the lower excited state (5D_0) or the ground state (7F_0). The activation energy for excitation into the CTS is lower for 5D_1 (E_{a2}) compared to 5D_0 (E_{a1}) and therefore quenching of the radiative decay from the 5D_1 level is stronger than from the 5D_0 level.

A second possible pathway to explain the temperature quenching of lanthanides, which cannot be explained by multiphonon relaxation, was first observed by Blasse et al.⁵⁰ and involves the role of the charge transfer state (CTS) in the temperature quenching of Eu^{3+} -activated oxides. A simplified representation of this phenomenon is given by Fonger et al.⁴⁶ using a normalized configuration coordinate diagram (Fig. 5b). When excitation occurs from the 5D states into the CTS it can thermalize rapidly to the bottom of the CTS after which it can non-radiatively decay to lower lying 5D states or the ground state via the intersection of the parabolas. For this phenomenon to occur, the CTS should be positioned at relatively low energies so thermal energy is sufficient to excite an electron from a 5D state to the intersection with the CTS. This process can shift the 5D populations to lower 5D states or even back to the ground state. As higher 5D states are positioned at higher energies and lie closer to the CTS ($E_{a1} > E_{a2}$), emissions from these states are quenched sequentially in the order 5D_3 , 5D_2 , 5D_1 , 5D_0 with increasing temperature. This quenching order indeed is a better representation of the experimental results for the quenching of lanthanide excited-states compared to the explanation in figure 4.⁴⁶

The opposite is also possible as the 5D states of europium, in activated oxides, can receive energy via the CTS of the absorbing groups when their energy levels lie close together. To reach high efficiencies for the Eu^{3+} luminescence, the absorption and energy transport in the host lattice is important as the energy absorbed at the absorbing groups should be transferred to the Eu^{3+} ion. Dexter et al.⁵¹ and Blasse and Brill⁵⁰ have shown that this energy transfer from absorbing groups to the rare earth ion is regulated by exchange processes and that the probability of this transfer is dependent on orbital overlap between host lattice and Eu^{3+} ion. They suppose that this overlap is strongly correlated with the angle between the center of the absorbing group, the O^{2-} ion and the rare earth ion. Therefore, exchange of energy from the absorbing group via the O^{2-} ion is dependent on the position of the CTS and thus the crystal structure.⁵⁰

3 EXPERIMENTAL METHODS

3.1 Catalyst synthesis

The EuOCl catalyst under study was synthesized based on the method described by Lercher et al.⁵² for the production of LaOCl. The europium (III) chloride salt ($\text{EuCl}_3 \cdot 6\text{H}_2\text{O}$, Alfa Aesar 99.9%) was dissolved in ethanol (absolute, VWR) followed by the dropwise addition of a small excess ammonium hydroxide (Fischer Scientific, 25% in H_2O) under rigorous stirring. The precipitate was washed and centrifuged twice with ethanol using a Rotina 380 centrifuge (Hettich) for 3:30 minutes at 3500 rpm. Finally, the obtained substance was dried for 3 hours at 80 °C to evaporate the ethanol and then calcined for 3 hours at 500 °C in a static air oven (Nabertherm) using a ramp rate of 5 °C/min. The calcined catalyst was pressed with a mechanical press (Specac) at 6 bar and then sieved (Retsch) to obtain the right catalyst sieve fraction (75 – 125 or 212 – 425 μm).

3.2 Catalyst characterization

X-ray diffraction (XRD) patterns were obtained with a Bruker-AXS D8 Advance Phaser powder X-ray diffractometer in Bragg–Brentano geometry, using $\text{Cu K}\alpha_{1,2} = 1.5406 \text{ \AA}$, operated at 40 kV. The measurements were carried out between 22 and 65° using a step size of 0.05° and a scan speed of 1 s, with a 2 mm slit for the source.

Operando photoluminescence spectra were collected using a 532 nm laser (AvaRaman-532 Hero-Evo) with a laser output of 50 mW and a spectral resolution of 10 cm^{-1} . The laser was equipped with an AvaRaman-PRB-FC-532 probe able to withstand temperatures of up to 500 °C. All spectra were collected using the Avasoft 8 software.

Transmission electron microscope images were taken on a FEI Tecnai 20 microscope operating at 200kV.

3.3 Catalytic testing

All *operando* photoluminescence experiments were performed in a lab scale continuous-flow fixed-bed quartz reactor. In most experiments the quartz reactor was filled with ~500 mg of the EuOCl catalyst. The reactor was placed in the middle of the oven with the laser aimed at the middle of the catalyst inside the reactor.

Operando photoluminescence spectra were collected every 30 seconds by tuning the number of averages, while the integration time was set to ensure sufficient, but not saturated, signal (at least 50% of saturation value). Collected spectra were converted from wavelength to wavenumber, baseline corrected, normalized and the $^5\text{D}_0$ peaks were deconvoluted using python (S2 and S4). Reaction conditions during experiments were controlled with lab view linked to the heat tracing (West 6100+) and EL Flow mass flow controllers (Bronkhorst), connected to the individual gasses (N_2 , O_2 , HCl , CH_4 and He). The chlorination of the catalyst was performed at 350 °C, dechlorination at 500 °C and oxychlorination experiments at 475 °C. Heating of the catalyst was done at a ramp speed of 15 °C/min under N_2 flow of 20 ml/min. During dechlorination and oxychlorination experiments, the amount of formed products were measured with a Trace 1300 Gas Chromatograph (Thermo Scientific, GAS) using the Chromeleon console software and nitrogen as internal standard.

4 RESULTS AND DISCUSSION

To monitor the local temperature of our EuOCl catalyst during the MOC reaction, it is important to establish boundary conditions under which temperature measurements are reliable. To find such conditions, first the synthesized EuOCl catalyst was characterized to check whether the correct catalyst was synthesized. Then, the thermometer performances of the synthesized catalyst in an inert environment were analyzed. Followed by the investigation of the effect of MOC reaction conditions on those thermometer performances. Tuning the operating conditions led to boundary conditions under which these effects were minimized, and temperature measurements were possible. With the established boundary conditions the temperature was monitored during several MOC experiments to study the effect of the reaction gas concentrations and the effect of the cold inflow of reaction gasses on the local temperature of the catalyst.

4.1 Catalyst characterization

The synthesized europium catalyst was characterized by comparing its XRD pattern with that of reference EuOCl (ICDD 04-009-9660) and reference $\text{EuCl}_3 \cdot 6\text{H}_2\text{O}$ (ICDD 01-083-9965) patterns (Fig. 6). The diffractogram clearly shows all of the EuOCl reference peaks with high intensity. EuOCl was thus synthesized with high purity.

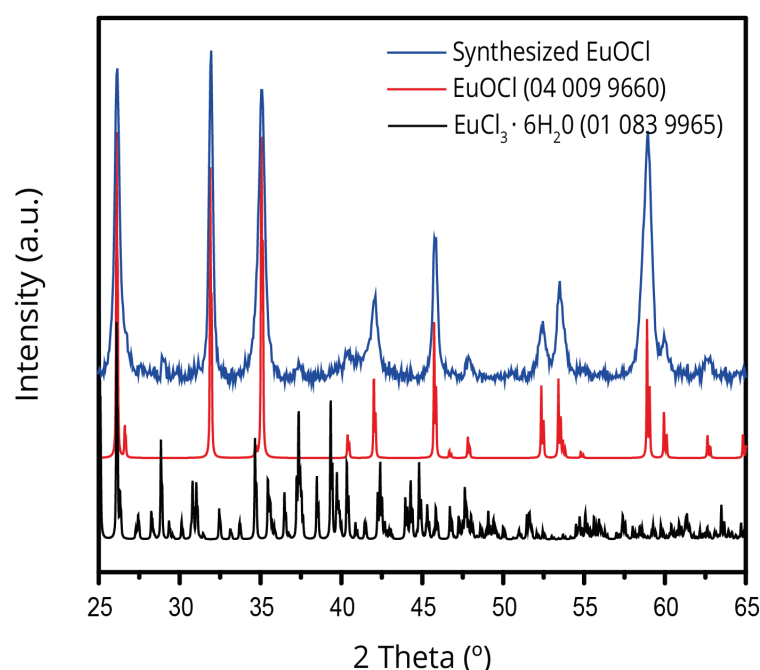


Figure 6. X-ray diffraction pattern of synthesized EuOCl catalyst together with EuOCl and $\text{EuCl}_3 \cdot 6\text{H}_2\text{O}$ references. The pattern of the synthesized catalyst matches well with the EuOCl reference.

4.2 EuOCl as thermometer in inert environment

Before temperature measurements with EuOCl under MOC reaction conditions were studied, the viability of EuOCl as a thermometer under inert environment was investigated. A viable band shape thermometer shows Boltzmann equilibrium between its two thermally coupled states. Therefore, all peaks of the luminescence emission spectrum of EuOCl were assigned to either $^5\text{D}_0$ or $^5\text{D}_1$ transitions. Then, a viable (group of) peak(s) was chosen for both the $^5\text{D}_0$ and $^5\text{D}_1$ intensity. Finally, the $^5\text{D}_1/^5\text{D}_0$ luminescence intensity peak ratio was calculated at temperatures ranging from 300 to 500 °C to make a calibration for the $^5\text{D}_1/^5\text{D}_0$ ratio versus the temperature in an inert environment.

Figure 7 shows the luminescence emission spectrum of EuOCl at 300 and 500 °C. The peaks in the spectrum were assigned, based on literature (S1), to transmissions originating from one of the two thermally coupled states.⁵³ At 500 °C compared to 300 °C the 5D_1 emissions (blue) were relatively more intense than the 5D_0 (gray) emissions. This result was expected as the Boltzmann distribution between the two thermally coupled states is temperature dependent (eq. 6). At higher temperatures the population in the 5D_1 state increased compared to the 5D_0 state and thus so did the emission intensity (eq. 7, 9).

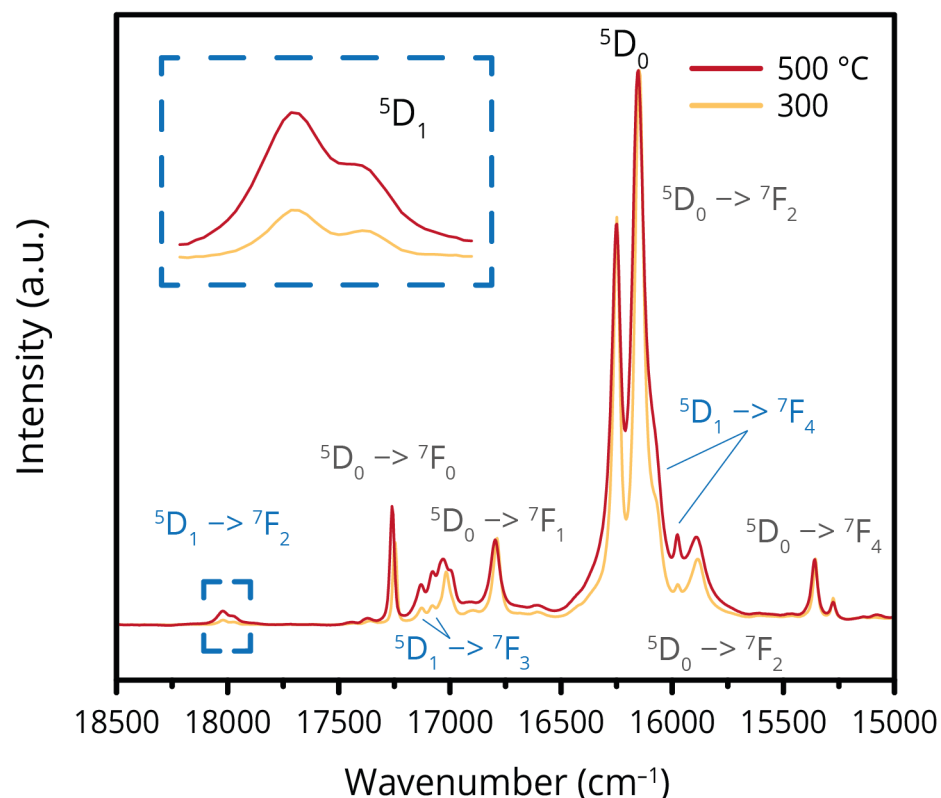


Figure 7. Normalized spectra of as synthesized EuOCl catalyst from 15000 to 18500 cm^{-1} at 300 and 500 °C. The peaks are assigned to their corresponding energy transitions. Peaks at $\sim 18000 \text{ cm}^{-1}$ were used as 5D_1 intensity (blue) and peaks at 16100 and 16250 cm^{-1} were used as 5D_0 intensity for the calculation of the luminescence intensity peak ratio used for temperature determination.

This temperature dependent $^5D_1/ ^5D_0$ peak intensity ratio was used for temperature measurements using band shape thermometry. It was important that a (group of) peak(s) was chosen for each thermally coupled state, for which the signal is maximized and overlap with the opposite state is minimized. When the signal for one of the (groups of) peaks is too low the signal to noise ratio will result in inaccurate temperature measurement. When there is overlap between peaks of the opposite states, a systematic error can be introduced to the temperature measurements.

In this study, the peaks at $\sim 18000 \text{ cm}^{-1}$ were used as 5D_1 intensity and the peaks at ~ 16150 and $\sim 16300 \text{ cm}^{-1}$ were used as 5D_0 intensity. The 5D_0 peaks were highly intense but did overlap with peaks belonging to 5D_1 emissions and can therefore introduce a systematic error to the temperature measurements. This systematic error was circumvented by deconvolution of the peaks in the range 15500 – 16500 cm^{-1} . The peaks were deconvoluted with a Lorentzian peak fit (S2) and after deconvolution only the peak area of the 5D_0 peaks at ~ 16150 and $\sim 16300 \text{ cm}^{-1}$ was used for the peak intensity ratio calculations. Peak deconvolution was only required for

the 5D_0 peaks due to the overlap with the 5D_1 emissions, for the 5D_1 peaks at $\sim 18000\text{ cm}^{-1}$ integrating over the peaks was sufficient as there was no overlap with 5D_0 emissions.

To find the correlation between the peak intensity ratio and the temperature a fresh EuOCl catalyst was ramped from 300 to 500 °C with a ramp of 1 °C/ min under inert environment and luminescence spectra were collected every minute. Figure 8a shows the collected luminescence emission spectra. The 5D_1 peaks (blue square) increased in intensity proportional to the temperature, while the 5D_0 peaks did not change significantly. Figure 8b visualizes the calculated I^5D_1/I^5D_0 ratio (red dots) versus the temperature in a plot. The I^5D_1/I^5D_0 ratio increased proportional to the temperature. The ΔE value of the catalyst was calculated by rewriting the Boltzmann equation (eq. 9) to (eq.17):

$$\Delta E = -0.695 * (T(^{\circ}\text{C}) + 273) \ln \left(\frac{I_2/I_1}{c} \right) \quad [17]$$

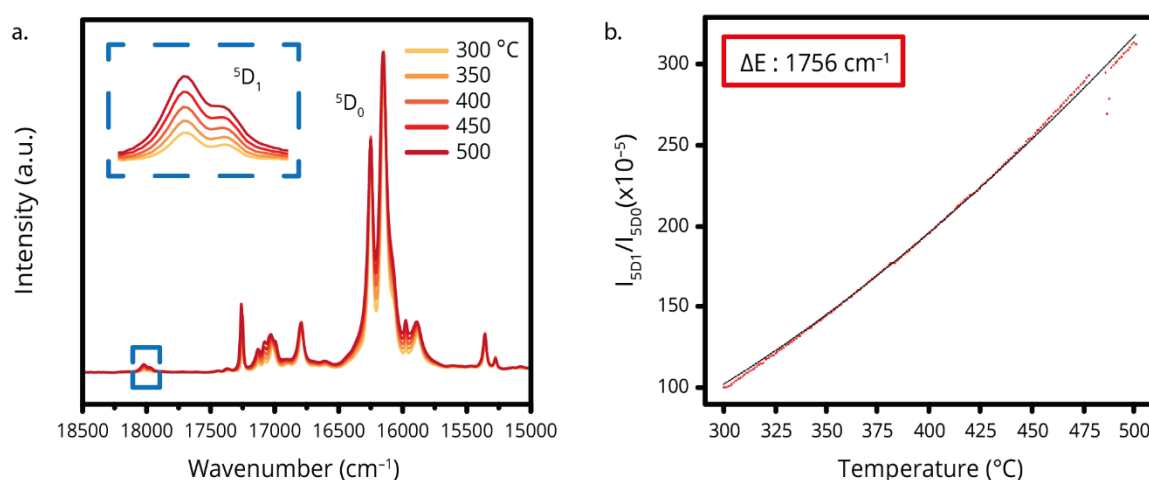


Figure 8. (a) Luminescence spectra of EuOCl plotted for 15000 – 18500 cm^{-1} in the temperature range 300 - 500 °C. (b) The calculated I^5D_1/I^5D_0 ratio from the spectra in a is plotted versus the temperature. The ΔE value was calculated using a Boltzmann fit (black line).

With the Boltzmann fit (black line) a ΔE value of 1756 cm^{-1} was found. This calculated value matched well with the theoretical energy gap between the 5D_1 and 5D_0 excited state of europium of $\sim 1780\text{ cm}^{-1}$.⁴⁹ The temperature of EuOCl could therefore be accurately determined under an inert environment using this fit.

Now that the viability of EuOCl as a thermometer was verified under an inert environment, its performances could be analyzed. In figure 9a the relative sensitivity (eq. 12) of europium is compared with several other rare earth metals, often used for band shape thermometry. From these rare earth metals europium has the highest ΔE value, it therefore also has the highest relative sensitivity. The high ΔE value of europium results in a thermal population of its higher excited state, 5D_1 , approaching zero at low temperatures. Although, this offers a high sensitivity, a drawback is that emission from this state is also very limited and therefore the signal to noise ratio is bad at lower temperatures. On the other hand, at high temperatures the thermal population in the 5D_1 level is very high resulting in only small changes with temperature and thus a low sensitivity. With the Boltzmann fit from figure 8b and the equation for the temperature uncertainty (eq. 13), the uncertainty in the temperature was simulated for a different number of counts. Figure 9b shows the estimated temperature uncertainty for europium in the temperature range 0 – 1000 °C for a varying number of averages per measurement (n). The temperature uncertainty was high at temperatures close to 0 °C and

increased in absolute terms at elevated temperatures. In relative terms the change in the uncertainty was much smaller. Note however that a constant number of photons was assumed over the whole temperature range, while the number of detected photons actually decreased with temperature. The actual slope in the temperature uncertainty is therefore steeper when going up in temperature. When the number of averages, or total counts per measurement, was increased the temperature uncertainty decreased according to the Poisson distribution with \sqrt{n} .⁴² At low temperatures europium is thus sensitive but inaccurate, while at high temperatures it is insensitive but accurate as a thermometer. Europium is both accurate and sensitive only in a certain temperature range. In the temperature range of interest for the MOC reaction, 300 – 500 °C, europium is both accurate and sensitive as a thermometer.

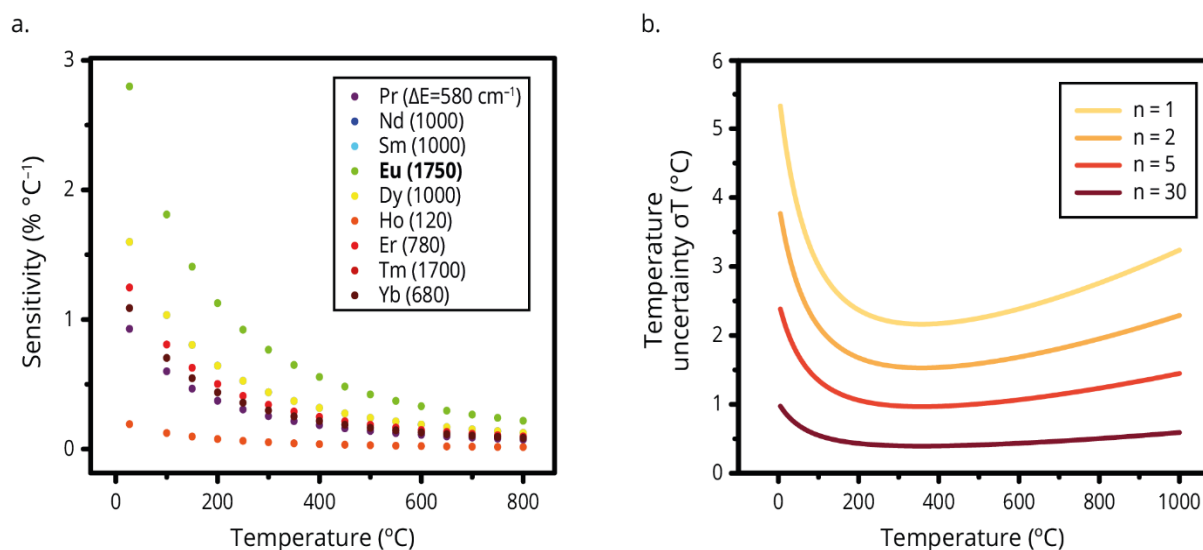


Figure 9. Thermometer performances (a) Relative sensitivity (eq. 12) of commonly used lanthanide thermometers is plotted over the temperature range 0 – 800 °C. (b) Simulation of the temperature uncertainty for EuOCl (eq. 13), based on the Boltzmann fit in figure 8b, with a varying number of averages (n) for each separate measurement.

4.3 Applicability of EuOCl as thermometer under MOC reaction conditions

It was shown that EuOCl is a viable thermometer in the temperature range of interest for the MOC reaction under an inert environment. However, the performances of the thermometer can deteriorate drastically under reaction conditions as the state of the catalyst can change constantly. These effects on the state of the catalyst were investigated by studying the individual reaction steps of the MOC reaction. As discussed previously, the MOC reaction cycle consists of three steps: (I) chlorination of the catalyst, (II) activation of chlorine and (III) the dechlorination of the catalyst. The activation of chlorine with oxygen occurs on the surface and not in the bulk, it was therefore invisible in the luminescence spectrum. During chlorination and dechlorination the state of the catalyst did change, which could affect the results found under inert environment. Therefore, these individual steps of the MOC reaction, chlorination and dechlorination, were investigated to find operating conditions that minimize these effects and enable reliable temperature measurements during the MOC reaction. First, measurements need to be representative for the whole sample therefore chlorination gradients over the reactor bed were prevented. Then, the effect of thermal quenching on the luminescence signal of the chlorinated catalyst was studied. Followed by the investigation of the effect of bulk chlorination on the reliability of temperature measurements.

4.3.1 Homogenous catalyst chlorination

To study the effect of the state of the catalyst on the luminescence signal it needs to be homogenous over the catalyst bed, otherwise collected spectra are not representative for the whole sample. EuOCl was chlorinated for 2h at $350\text{ }^\circ\text{C}$ and then luminescence and Raman spectra were collected at room temperature at different heights in the reactor (top, middle and bottom) (Fig. 10b). Afterwards the different parts of the sample were separated and measured with XRD. Figure 10 shows the luminescence spectra, Raman spectra and XRD patterns for the different parts of the reactor together with references for EuOCl and EuCl_3 for each of the techniques.

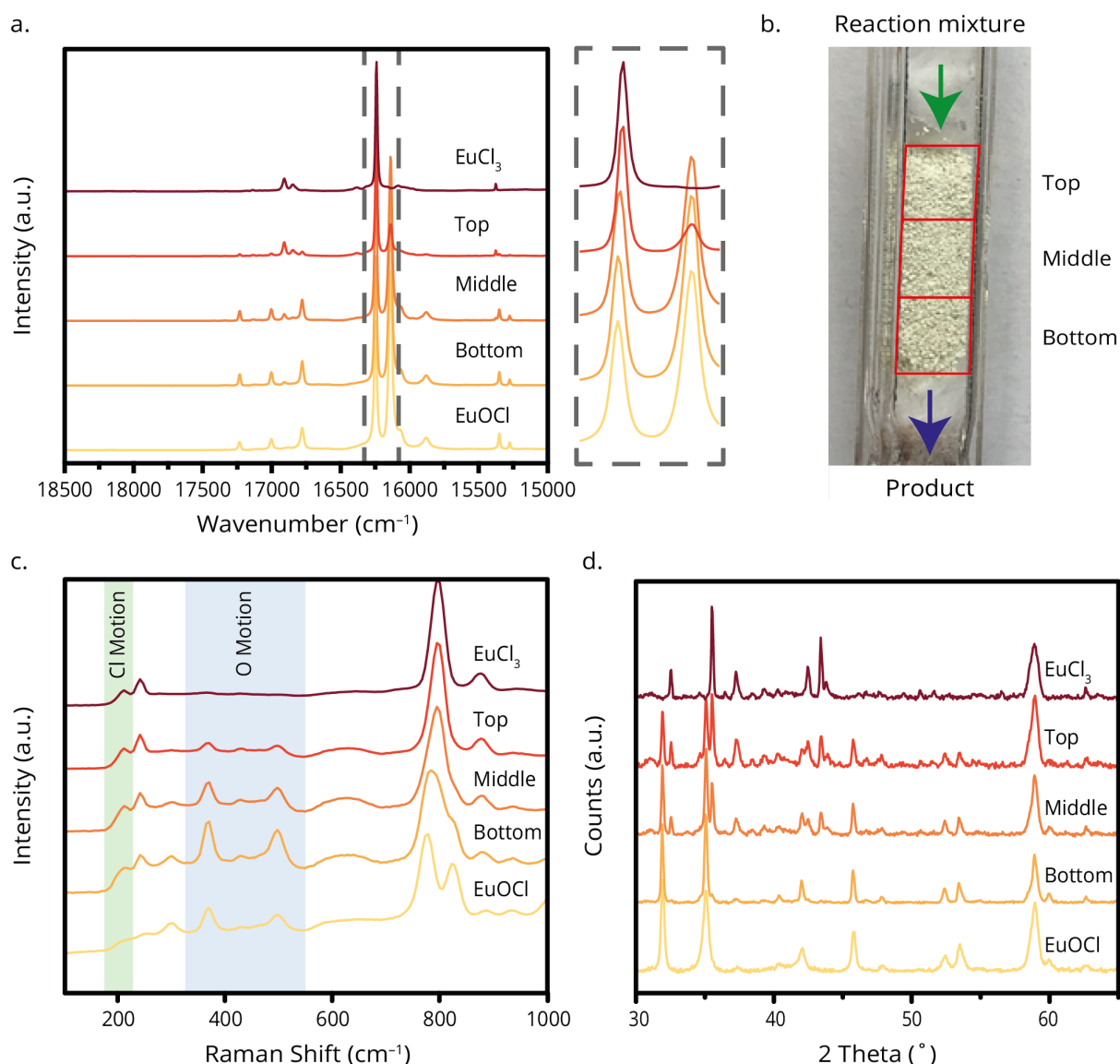


Figure 10. (a) Luminescence spectra of different parts of the reactor plotted together with reference spectra of EuOCl and EuCl_3 for $15000 - 18500\text{ cm}^{-1}$. (b) Image of the reactor with assigned parts of the reactor. The gas inflow is from the top of the reactor and the product is collected at the bottom. (c) Raman spectra of the different parts of the reactor plotted together with reference spectra of EuOCl and EuCl_3 for $100 - 1000\text{ cm}^{-1}$. The Cl motion peak is positioned at $\sim 200\text{ cm}^{-1}$ and the O motion peaks are positioned at ~ 390 and $\sim 510\text{ cm}^{-1}$. These peaks can be used for the maximum phonon energy of the lattice. (d) XRD patterns of the different parts of the reactor together with reference patterns of EuOCl and EuCl_3 . The luminescence spectra, Raman spectra and XRD patterns all show a clear chlorination gradient over the reactor when compared to the references. The top of the reactor, where the inflow of reaction gasses is, has a higher degree of chlorination than the bottom.

The luminescence data in figure 10a shows the collected spectra for the different parts of the reactor. The spectra look different over the sample. The spectrum of the top of the reactor looks

like the EuCl_3 reference, while the spectrum of the bottom looks like the EuOCl reference. This shows that there was a chlorination gradient over the reactor. The top of the reactor, where the gas inflow was, had a higher degree of chlorination and the degree of chlorination decreased going down the reactor. This conclusion was verified by the Raman spectra shown in figure 10c. In figure 10c the peak at 200 cm^{-1} belongs to the motion of chlorine and the peaks at approximately 380 and 520 cm^{-1} belong to the motion of oxygen. The spectra from top to bottom of the reactor show that the Cl motion peak decreased in intensity, while the O motion peaks increased in intensity. The XRD patterns in figure 10d show a changing crystal structure going down the reactor, which coincides with the changes shown by luminescence and Raman. Comparing the diffractograms with the references, EuCl_3 (ICDD 04 007 3099) and EuOCl (ICDD 04 009 9660), shows that a sum of both phases was present over the whole sample. At the bottom of the reactor there was only a minor EuCl_3 phase, but this phase became more dominant going to the top of the reactor.

From the luminescence, Raman and XRD data it was shown that there is a chlorination gradient over the reactor. This is undesired as spectra collected at a single position in the reactor were not representative and therefore drawing conclusions on the effect of the degree of chlorination was difficult. A possible reason for this chlorination gradient was a strong interaction between the gas flow and the catalyst resulting in a pressure drop over the reactor bed. Therefore, the flows were increased from 20 to 60 ml/min (HCl concentration constant at 20%) to decrease residence time and the catalyst sieve fraction was increased, from $75 - 125\text{ }\mu\text{m}$ to $212 - 425\text{ }\mu\text{m}$, to reduce the interaction between the gas flow and the catalyst. Figure 11 shows the luminescence spectra of a fresh EuOCl catalyst, with a $212 - 425\text{ }\mu\text{m}$ sieve fraction, after 2 h of chlorination at $350\text{ }^\circ\text{C}$ with 60 ml/min flow. The peak at $\sim 16150\text{ cm}^{-1}$ is slightly less intense at the top of the reactor bed compared to the middle and bottom. This shows that there still was a small chlorination gradient over the reactor bed. However, the gradient was drastically reduced compared to the smaller sieve fraction and lower flows (Fig. 10a).

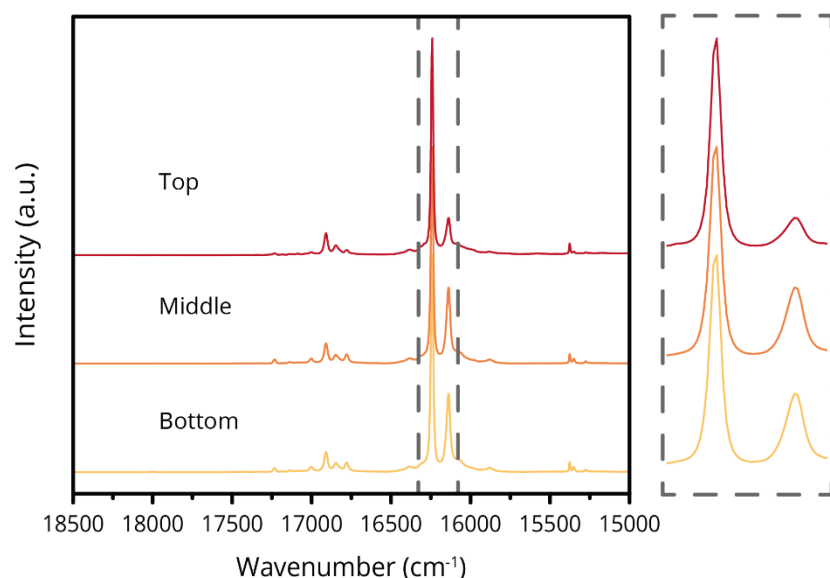


Figure 11. A EuOCl catalyst with a sieve fraction of $212 - 425\text{ }\mu\text{m}$ was chlorinated for 2 h at $350\text{ }^\circ\text{C}$ with a flow of 60 ml/min (20% HCl). The catalyst was cooled down to room temperature and luminescence spectra of the chlorinated catalyst were collected at different parts of the reactor.

Homogenous chlorination over the reactor bed was needed for reliable temperature measurements. Therefore, a sieve fraction of $212 - 425\text{ }\mu\text{m}$ and higher flows during chlorination of 60 ml/min (20% HCl) were used for further experiments.

4.3.2 The thermal quenching of the luminescence signal

With a homogenous chlorination over the reactor bed the effect of temperature on the chlorinated catalyst could be studied. Therefore, the chlorinated catalyst, from figure 11, was heated to 350 °C in an inert environment and luminescence spectra were collected. Figure 12 shows the luminescence spectra for the temperature ramp 30 – 350 °C.

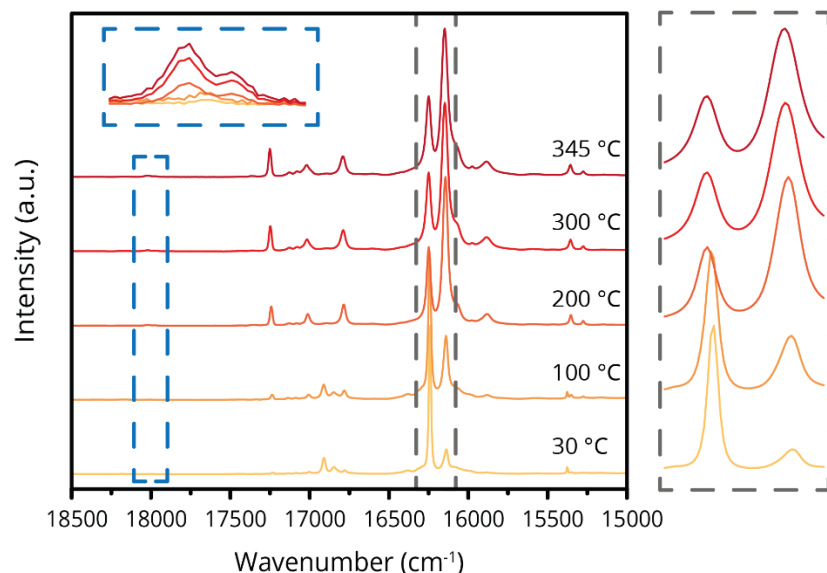


Figure 12. Luminescence spectra of the chlorinated catalyst collected during the temperature ramp from 30 to 350 °C under inert environment. The spectra change from being similar to EuCl_3 to being similar to EuOCl at higher temperatures.

When the temperature increased the luminescence spectra changed drastically. The $^5\text{D}_1$ peaks increased in intensity, the characteristic EuCl_3 peaks in the range 16750 - 17250 cm^{-1} and 15250 – 15500 cm^{-1} became undetectable, while characteristic EuOCl peaks arose, and finally the $^5\text{D}_0$ peaks changed. Overall, the spectrum changed from a spectrum similar to EuCl_3 at low temperatures to a spectrum similar to EuOCl at high temperatures. There are two possible explanations for this phenomenon, (i) either the catalyst lost chlorine upon heating or (ii) the EuCl_3 signal was quenched at elevated temperatures. The loss of chlorine seems unlikely as the catalyst was in an inert environment. To verify this assumption the catalyst was cooled to room temperature after the ramp and the spectra before and after heating of the catalyst were compared. Figure 13 shows the spectra of the different parts of the reactor after the temperature ramp. The spectra look similar to EuCl_3 and have not changed significantly from the spectra pre temperature ramp in figure 11, which would be expected when chlorine was lost during the ramp. Thus, the loss of chlorine during heating of the catalyst was refuted.

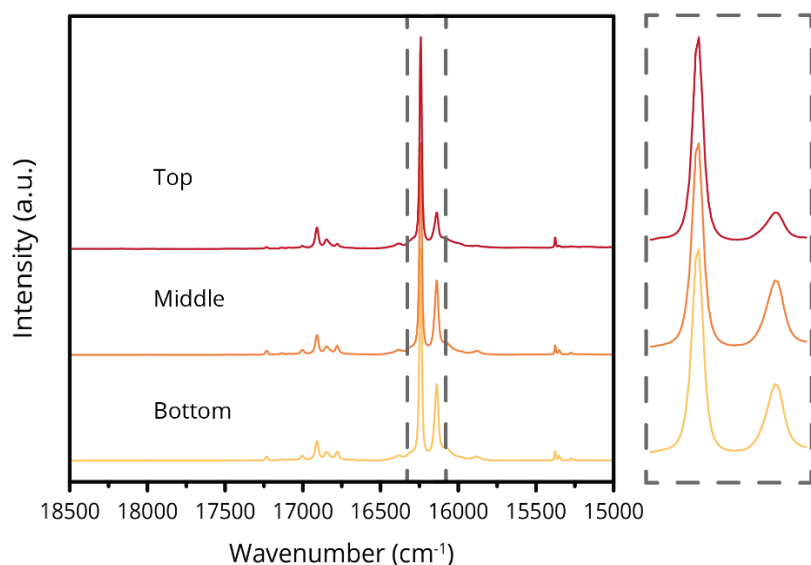


Figure 13. Luminescence spectra of the chlorinated catalyst after the temperature ramp from 30 to 350 °C, collected at room temperature at different heights in the reactor. The spectra look similar to EuCl_3 thus no chlorine has been lost upon heating the catalyst under inert environment.

Another explanation for the changes in the luminescence spectra during heating of the chlorinated catalyst could be the thermal quenching of EuCl_3 . When EuCl_3 was quenched at elevated temperatures and therefore became undetectable, while the small amount of the EuOCl phase remained visible, the EuOCl would be dominant in the luminescence spectra and this could explain the changes in the spectra upon heating. This assumption was strengthened by the observation that the overall signal decreased drastically upon heating of the sample. The quenching behavior of EuOCl and EuCl_3 was further investigated by the analysis of the pure phase using the excitation spectra and luminescence lifetimes over a variety of temperatures. To find the origin of the drastic decrease in overall signal, excitation spectra of pure EuOCl and EuCl_3 at temperatures between 30 and 500 °C were compared.

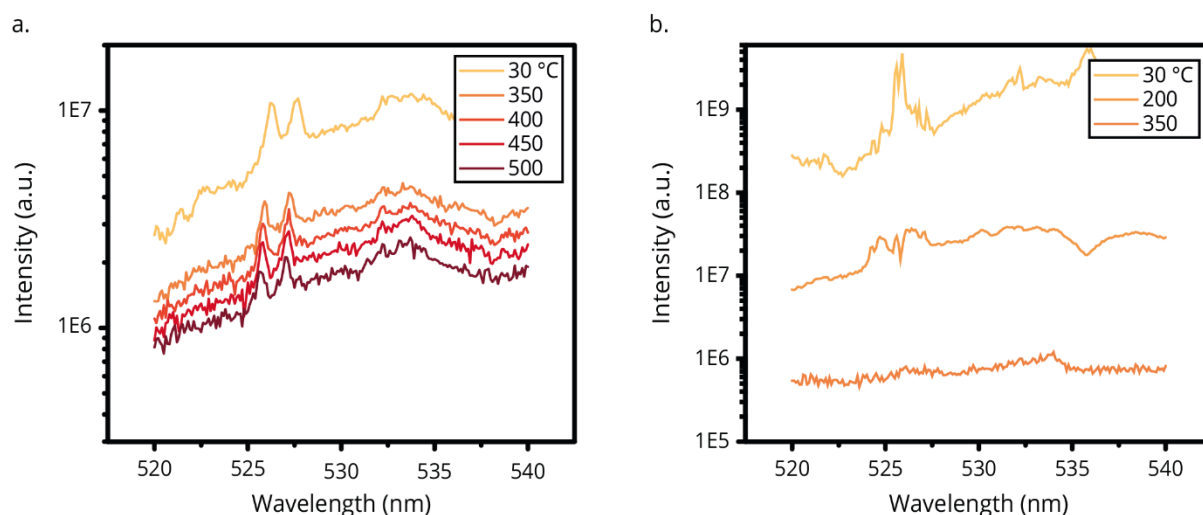


Figure 14. Excitation spectra with the intensity plotted versus the excitation wavelength at different temperatures for (a) EuOCl and (b) EuCl_3 . The signal of the excitation spectrum of EuOCl decreases by ~60% when the temperature is increased from 30 to 500 °C. The signal of the excitation spectrum of EuCl_3 decreases much faster as ~99% of the signal is lost when the temperature is increased from 30 to 350 °C. The shape of the EuCl_3 excitation spectrum also changes significantly upon heating.

Figure 14 shows the excitation spectra of EuOCl and EuCl_3 . The excitation spectra of EuOCl had the exact same shape for all temperatures, while the excitation spectra of EuCl_3 had drastically changed and were a lot noisier at higher temperatures. A steady decline in the

intensity of the signal for EuOCl was visible with increasing temperature. An increase in temperature from 30 to 500 °C resulted in a decrease in signal of approximately 60%. The decrease in intensity of the EuCl₃ signal however showed a much faster decline. A temperature increase from 25 to 350 °C now resulted in a decrease in signal of more than 99%. The decrease in intensity for both samples was a result of an increase in the temperature dependent non-radiative decay. The stronger thermal quenching of the EuCl₃ signal compared to EuOCl could explain the changes in the luminescence spectra of the chlorinated catalyst during heating. This observation was studied by luminescence lifetimes measurements of EuOCl and EuCl₃. During these measurements EuOCl and EuCl₃ were excited into the ⁵D₀ level and luminescence decay was measured at ~16100 cm⁻¹. The EuOCl measurements were performed at temperatures in the range 30 - 500 °C and the EuCl₃ measurements in the range 30 – 350 °C. Figure 15a shows the luminescence lifetimes plots for EuOCl. The EuOCl decay plots show that the decay rate increased with temperature and that there was single exponential decay. In figure 15b the change in the decay rate with temperature for EuOCl is visualized in a plot. The decay rate was calculated with a single exponential fit and plotted versus the temperature. The decay rate increases to ~280 ms⁻¹ at a temperature of 500 °C. As the radiative decay rate is considered temperature independent the increase in the decay rate was a result of an increase in the temperature dependent non-radiative decay rate. Figure 15c shows the luminescence lifetimes plots for EuCl₃.

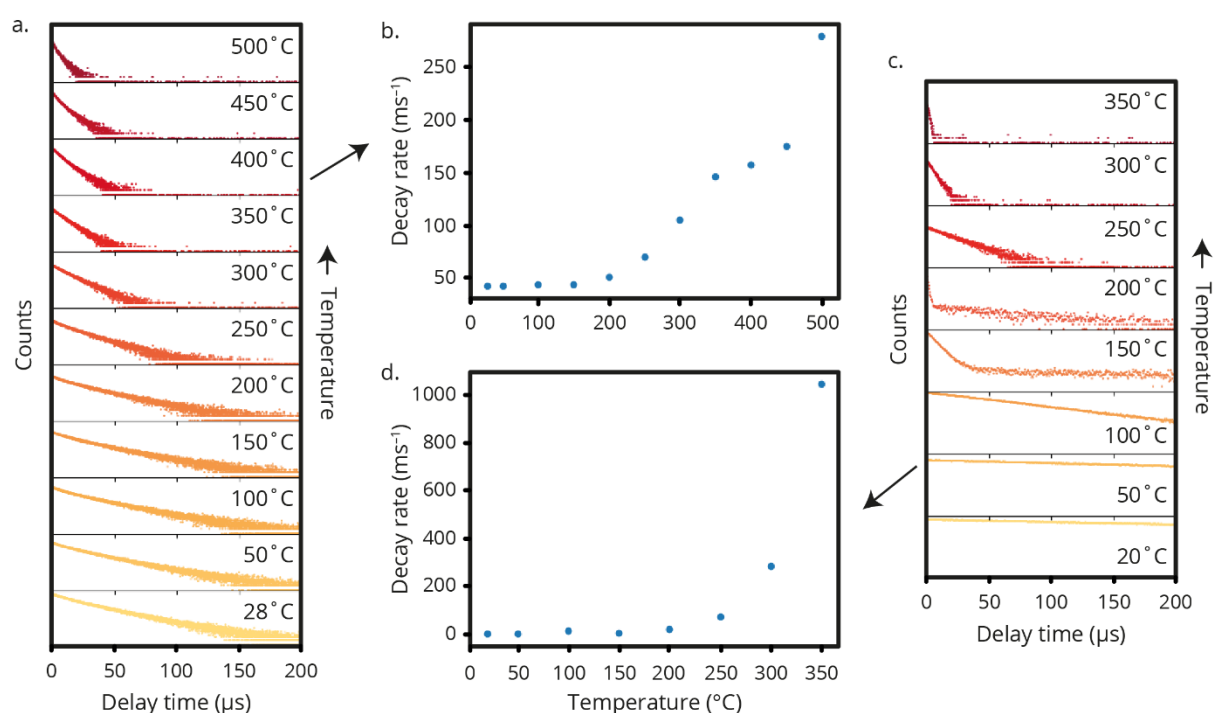


Figure 15. Luminescence lifetimes experiments at a variety of temperatures for (a, b) pure EuOCl and (c, d) pure EuCl₃. (a) The number of counts is plotted versus the delay time for temperatures in the range 28 – 500 °C for a pure EuOCl sample. The delay time shortens, and the decay rate thus increases, when the temperature is increased. (b) The decay rate was obtained from a. with a single exponential fit and plotted versus the temperature. The decay rate is constant till 150 °C this shows the temperature independent radiative decay. At temperatures higher than 150 °C the thermal energy is sufficient to excite electrons to the CTS enabling non-radiative decay to the ground state. The non-radiative decay rate increases exponentially with the temperature. (c) The number of counts is plotted versus the delay time for temperatures in the range 20 – 350 °C for a pure EuCl₃ sample. The EuCl₃ decay curves show bi-exponential decay for the measurements at 150 and 200 °C indicating an additional type of decay. Similar to EuOCl the delay time shortens, and the decay rate thus increases, when the temperature is increased. (d) The decay rate was obtained from c with a single exponential fit, because the faster decay formed only a small part of the total decay in a few measurements. Just as for EuOCl, the decay rate is constant till 150 °C this shows the temperature independent radiative decay. At temperatures higher than 150 °C the thermal energy is sufficient to excite electrons to the CTS enabling non-radiative decay to the ground state. The non-radiative decay rate increases exponentially with the temperature.

The decay rate of EuCl_3 increased with temperature just as for EuOCl , however EuCl_3 had biexponential decay at temperatures of 150 and 200 °C. The biexponential decay could be a result of a small phase change due to leakage of air into the reactor or belong to $^5\text{D}_1$ decay due to thermal excitation from the $^5\text{D}_0$ into the $^5\text{D}_1$ level. Although, EuCl_3 had biexponential decay at some of the higher temperatures, a single exponential fit was used to calculate the decay rates as the fast component formed only a small part of the total decay. Figure 15d shows the decay rate versus the temperature for EuCl_3 . The decay rate increased to $\sim 1000 \text{ ms}^{-1}$ at a temperature of 350 °C as a result of an increase in the non-radiative decay rate. Although, the increase in decay rate with temperature was significant for both samples, the decay for EuCl_3 ($\sim 1000 \text{ ms}^{-1}$ at 350 °C) was much faster than for EuOCl ($\sim 300 \text{ ms}^{-1}$ at 500 °C). Therefore, non-radiative decay was much more dominant for EuCl_3 than for EuOCl , which is in line with the conclusion drawn from the excitation spectra earlier. The stronger increase in the non-radiative decay rate with temperature for EuCl_3 than for EuOCl can be explained qualitatively according to the position of the CTS using the Mott-Seitz theory. Figure 16 shows an example of a possible representation of EuOCl and EuCl_3 in a configurate coordinate model. A CTS positioned at a lower energy or with a smaller r for EuCl_3 compared to EuOCl would result in a lower activation energy for excitation of an electron from the $^5\text{D}_0$ parabola to the intersection with the particular CTS after which it can non-radiatively decay to the ground state. Therefore, the required thermal energy for the non-radiative decay of an electron to the ground state would be lower for EuCl_3 (E_{a1}) than for EuOCl (E_{a2}). This results in the faster decay rate for EuCl_3 and the quenching of its signal at higher temperatures.

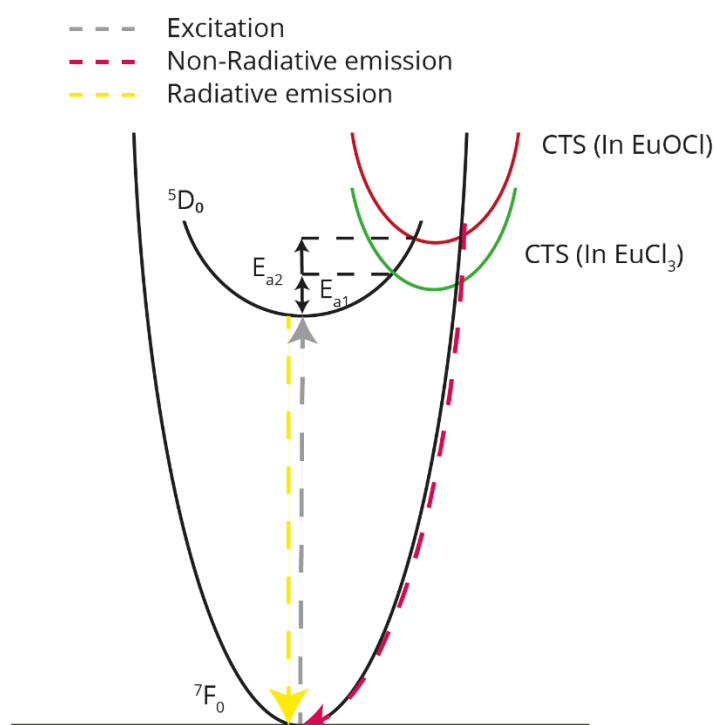


Figure 16. Configurative coordinate model for a possible explanation of the faster quenching of the EuCl_3 signal compared to the EuOCl signal. When the CTS is positioned at a higher energy level more thermal energy is required for non-radiative decay via the CTS to the ground state. Less thermal energy is thus needed to excite electrons from an excited state to the CTS of EuCl_3 , this results in a faster decay for EuCl_3 compared to EuOCl

Non-radiative decay would also be possible through multiphonon relaxation. To check whether this is possible in this case, the maximum phonon energy was obtained from the Raman spectra (Fig. 10c). The maximum phonon energy of EuCl_3 and EuOCl is $\sim 250 \text{ cm}^{-1}$ and $\sim 520 \text{ cm}^{-1}$ respectively. The samples were expected to be pure phases without impurities and therefore energy levels between the $^5\text{D}_0$ and $^7\text{F}_6$ were absent. To bridge the gap between $^5\text{D}_0$ and $^7\text{F}_6$

energy level ($\sim 12000 \text{ cm}^{-1}$), 48 and 23 phonons would be required for EuCl_3 and EuOCl respectively. The probability for multiphonon relaxation decreases proportional to the number of phonons needed and therefore multiphonon relaxation was very improbable in this case.

The spectra of the chlorinated catalyst thus changed due to the faster thermal quenching of EuCl_3 than for EuOCl . This resulted in almost complete quenching of EuCl_3 and a dominant EuOCl spectrum at elevated temperatures.

4.3.3 The effect of catalyst chlorination on the I^5D_1/I^5D_0 ratio and on the luminescence emission spectrum of europium

As chlorination induced significant changes in the spectrum of the EuOCl catalyst it is important to study this effect on the reliability of EuOCl as a thermometer. First, an additional parameter was introduced, which can detect when temperature determination becomes unreliable due to catalyst chlorination. Then, the I^5D_1/I^5D_0 ratio was studied during chlorination and dechlorination of the catalyst. Followed by, the effect of the chlorination temperature on the catalyst and its reliability as a thermometer. Finally, the required boundary conditions for reliable temperature measurements during the MOC reaction are discussed.

The I^5D_1/I^5D_0 ratio formed the basis for temperature measurements and therefore it was important that changes in the peak ratio as a result of changes in temperature were separated from those caused by changes in the degree of chlorination of the catalyst. An additional parameter was needed that can visualize changes in the state of the catalyst and can warn when temperature determination is unreliable. This parameters needed to be sensitive to changes in the state of the catalyst while being relatively insensitive to changes in temperature during the MOC reaction. This additional parameter was the intra level peak ratio calculated for the 5D_0 (blue line) and 5D_1 (green line) peaks. These intra level peak ratios describe relative changes in the spectrum and are given by (eq. 18, 19):

$$^5D_1 \text{ intra level peak ratio} = \int \text{peak 1} / \int \text{peak 2} \quad [18]$$

$$^5D_0 \text{ intra level peak ratio} = \int \text{peak 4} / \int \text{peak 3} \quad [19]$$

Figure 17 shows the peak areas that were used for the calculation of the 5D_1 (17a) and 5D_0 (17b) intra level peak ratios. The 5D_1 peaks were not deconvoluted because there was no overlap with other peaks opposed to the deconvoluted 5D_0 peaks.

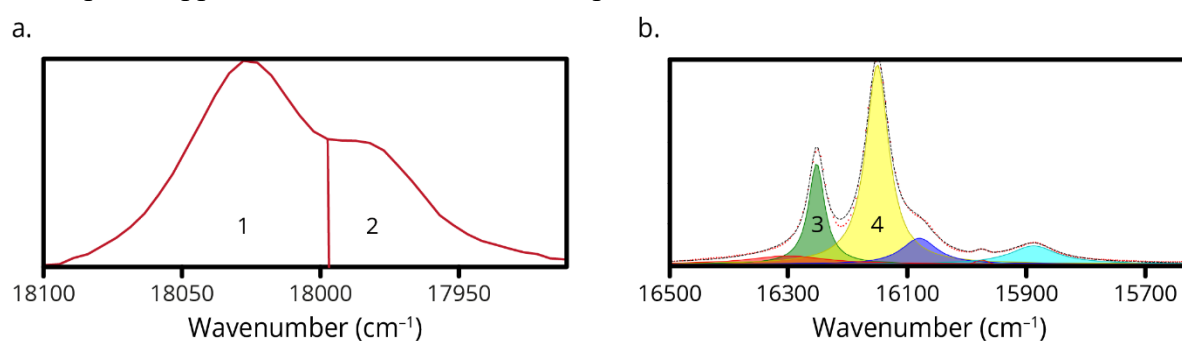


Figure 17. Visualization of the intra level peak ratios (a) for the 5D_1 peaks and (b) the deconvoluted 5D_0 peaks. The ratio peak 1/peak 2 and peak 4/peak 3 will be used to detect changes in the state of the catalyst.

The effect of chlorination on the I^5D_1/I^5D_0 ratio and the luminescence spectrum was studied by collecting luminescence spectra, while chlorinating a fresh EuOCl catalyst at $350 \text{ }^\circ\text{C}$. Figure 18a shows the collected spectra during chlorination over time. The intensity of both 5D_1 peaks and the 5D_0 peak at $\sim 16300 \text{ cm}^{-1}$ decreased in intensity during chlorination of the catalyst.

These peaks were all used for temperature measurements and chlorination could thus introduce an error to the calculated temperature. Figure 18b visualizes those changes in the I^{5D_1}/I^{5D_0} ratio and the intra level peak ratios in a plot. The I^{5D_1}/I^{5D_0} ratio decreased and both the intra level peak ratios increased when the catalyst was chlorinated. Therefore, when the intra level peak ratios increase during a MOC experiment this shows the catalyst is chlorinating and the state of the catalyst is changing, which makes temperature measurements unreliable.

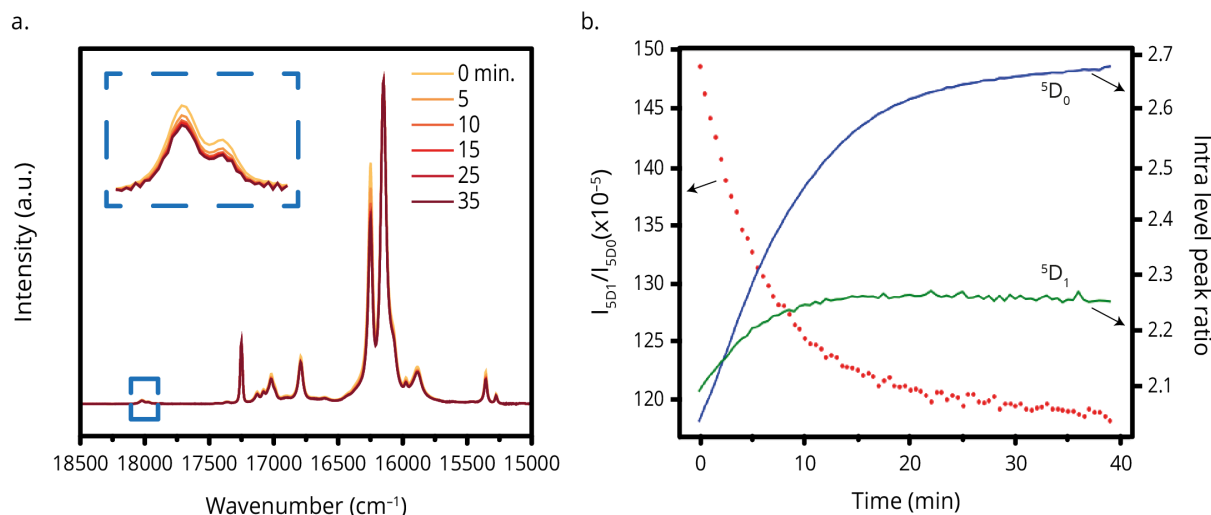


Figure 18. The effect of chlorination at 350 °C, with 60 ml/min (20% HCl), on the luminescence spectra of EuOCl. (a) During chlorination the 5D_1 peaks and the 5D_0 peak at 16300 cm^{-1} decrease in intensity. (b) The I^{5D_1}/I^{5D_0} ratio and intra level peak ratios are plotted versus the chlorination time. Upon chlorination the I^{5D_1}/I^{5D_0} ratio decreases, while the intra level peak ratios increase. When the intra level peak ratios increase during an experiment this is a sign that the catalyst is chlorinating and thus the state of the catalyst is changing.

After chlorination the catalyst was heated to 500 °C and while collecting luminescence spectra the catalyst was dechlorinated. Figure 19a shows the collected spectra during dechlorination at 500 °C over time. Now, the opposite was true compared to chlorination as the 5D_1 peaks increased in intensity. The 5D_0 peak at $\sim 16300 \text{ cm}^{-1}$ also changed however only slightly compared to the change during chlorination. In figure 19b those changes are visualized in a plot. The changes were indeed opposite to those in figure 18b as the I^{5D_1}/I^{5D_0} ratio increased and the intra level peak ratios decreased during dechlorination.

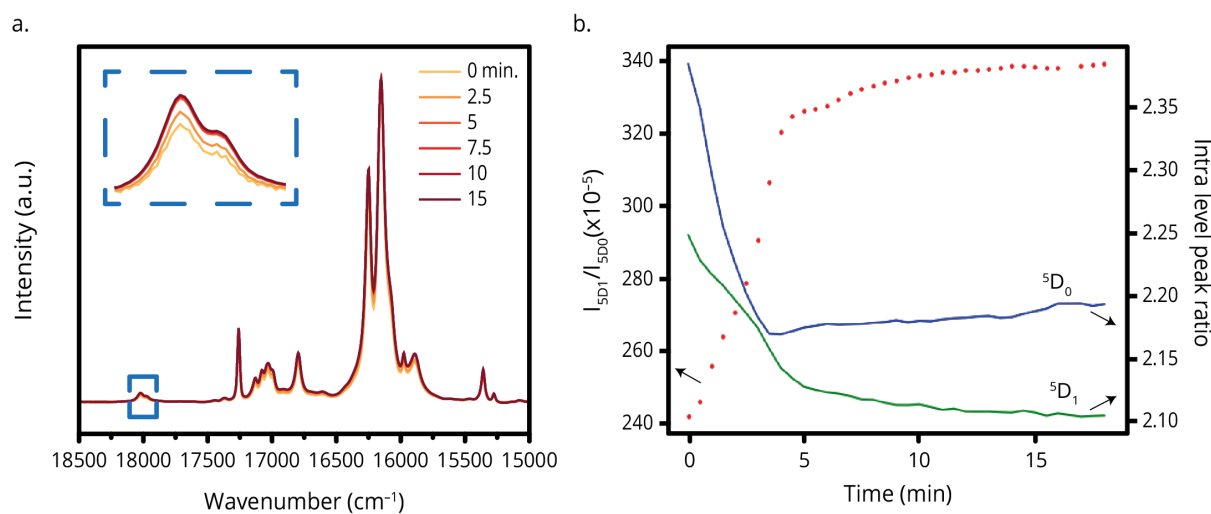


Figure 19. The effect of dechlorination at 500 °C, with $\text{N}_2 : \text{O}_2 : \text{HCl} : \text{CH}_4 : \text{He}$ flow of 1 : 1 : 0 : 2 : 16, on the luminescence spectra of the chlorinated EuOCl catalyst. (a) During dechlorination the 5D_1 peaks and the 5D_0 peak at 16300 cm^{-1} increase in intensity. (b) The I^{5D_1}/I^{5D_0} ratio and intra level peak ratios are plotted versus the dechlorination time. Upon dechlorination the I^{5D_1}/I^{5D_0} ratio increases, while the intra level peak ratios decrease. When the intra level peak ratios decrease during an experiment this is a sign that the catalyst is dechlorinating and thus the state of the catalyst is changing.

The intra level peak ratios before chlorination and after dechlorination did not match as would be expected if chlorination of the catalyst was irreversible and the intra level peak ratio would be completely independent of the temperature. This could be a result of irreversible changes in the catalyst due to chlorination and/or a result of the different temperatures used for chlorination (350 °C) and dechlorination (500 °C). The effect of temperature on the spectra was previously shown and is expected to be limited due to the strong thermal quenching of EuCl_3 . The reversibility of the catalyst chlorination was studied by doing 5 chlorination – dechlorination cycles at 350 °C and 500 °C respectively for 2 hours and measuring the amount of formed products during each of the dechlorination steps with the GC. With the amount of formed products the excess chlorine per europium was calculated for each cycle. Figure 20 shows the excess chlorine per europium versus the dechlorination time for each consecutive cycle.

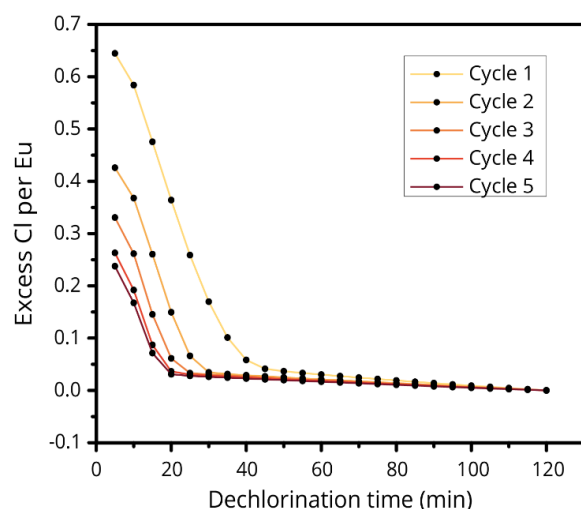


Figure 20. The excess Cl per Eu is calculated from the formed products during dechlorination. The excess Cl per Eu decreased with each cycle. This shows that chlorination and/ or dechlorination became more difficult with each cycle.

With each consecutive cycle the amount of excess chlorine on the catalyst decreased. This shows that chlorination and/ or dechlorination became more difficult with each consecutive cycle. A possible explanation for this observation is a decrease in the surface area of the catalyst with each cycle.⁵²

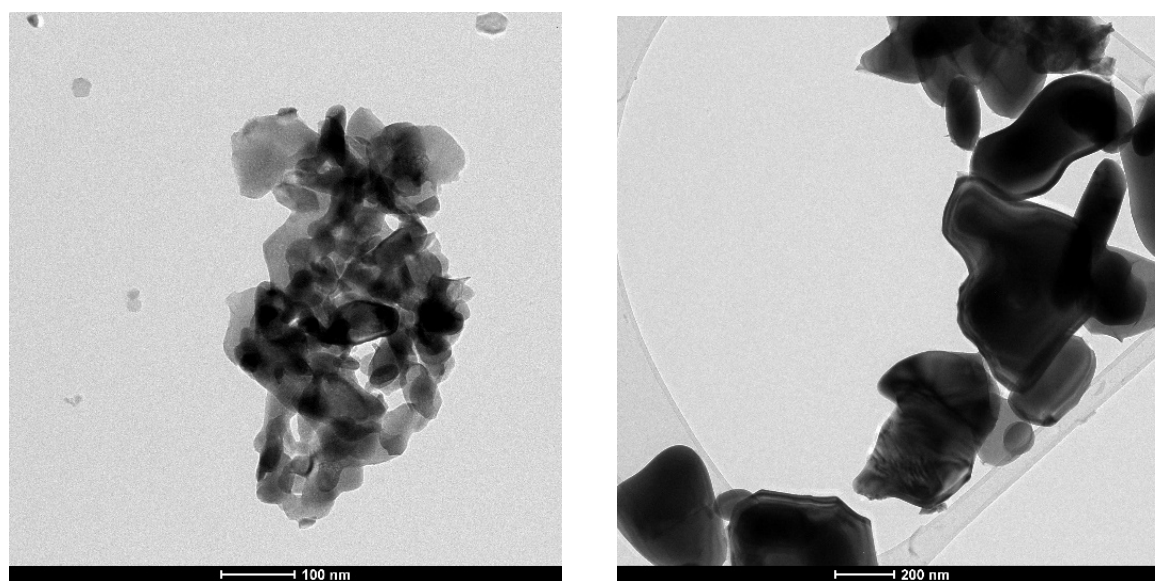


Figure 21. TEM images of (a) fresh EuOCl with defined particles of varying size and shape, and (b) chlorinated catalyst where particle agglomeration is clearly visible.

This assumption was confirmed by comparison of the TEM images before and after chlorination (Fig. 21a, b). Figure 21b shows particle agglomeration due to chlorination of the catalyst, which resulted in diffusion limitations and thus made chlorination and dechlorination of the catalyst more difficult. Bulk chlorination of the EuOCl catalyst was thus an irreversible process. As shown earlier chlorination affects the I^{5D_1}/I^{5D_0} ratio and the intra level peak ratios and was thus undesired for temperature measurements. Therefore, MOC reaction conditions were needed at which bulk chlorination of the catalyst was limited.

To find such conditions a fresh EuOCl catalyst was chlorinated at varying temperatures from $475\text{ }^\circ\text{C}$ to $350\text{ }^\circ\text{C}$ (with steps of $25\text{ }^\circ\text{C}$) starting from $475\text{ }^\circ\text{C}$. During the experiment cooling of the catalyst was done under inert environment. Figure 22 shows the I^{5D_1}/I^{5D_0} ratio and intra level peak ratios versus the time on stream. A change in the I^{5D_1}/I^{5D_0} ratio could either be a result of a temperature change or a change in the state of the catalyst. The intra level peak ratios did not change drastically during the inert cooling of the catalyst step and changes were thus the result of a change in the state of the catalyst. During the chlorination steps the I^{5D_1}/I^{5D_0} ratio decreased and the intra level peak ratios increased showing chlorination of the catalyst. The change in the ratios was proportional to the change in the degree of chlorination. The larger change in the ratios at lower temperatures thus showed a larger change in the degree of chlorination. This suggests that EuCl_3 was more stable at lower temperatures, which is a similar result as for the LaCl_3 catalyst used by Lercher et al.²⁰ During the chlorination step at $375\text{ }^\circ\text{C}$ both the I^{5D_1}/I^{5D_0} ratio and the intra level peak ratios stagnated. This observation was assigned to the saturation of the catalyst with chlorine, making further chlorination increasingly difficult.

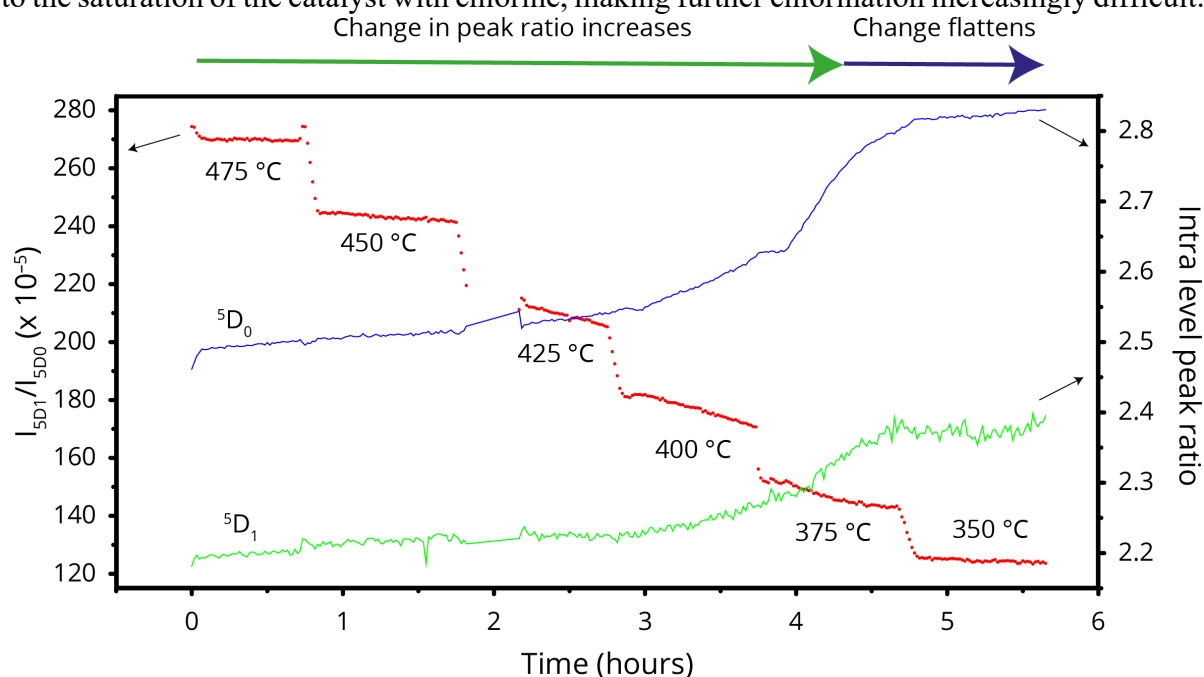


Figure 22. Luminescence I^{5D_1}/I^{5D_0} ratio and intra level peak ratios versus time on stream during chlorination at varying chlorination temperatures between 475 and $350\text{ }^\circ\text{C}$. The change in the I^{5D_1}/I^{5D_0} and intra level peak ratios shows the change in the state of the catalyst. From $475 - 375\text{ }^\circ\text{C}$ the changes increase showing a faster change in the state of the catalyst. This was assigned to chlorination favoring lower temperatures. Half-way through the $375\text{ }^\circ\text{C}$ step the change in the ratios stagnates this was assigned to the saturation of the catalyst with chlorine making further chlorination increasingly difficult.

The change in the ratios at $475\text{ }^\circ\text{C}$ was limited and therefore bulk chlorination could be drastically suppressed at reaction temperatures of $\geq 475\text{ }^\circ\text{C}$. To verify this observation the previous experiment was repeated with a constant temperature of $475\text{ }^\circ\text{C}$ and while collecting luminescence spectra. Figure 23a shows the I^{5D_1}/I^{5D_0} ratio and intra level peak ratios versus the time on stream of the 5 chlorination – dechlorination cycles. During chlorination (green)

the I^{5D_1}/I^{5D_0} ratio decreased and the intra level peak ratios increased. The opposite was true for dechlorination (yellow). Those results were the same as in figure 18 & 19. During the first chlorination cycle a quick increase in the intra level peak ratios was observed. In the consecutive cycles the intra level peak ratios increased in a stair like manner. The quick increase during the first chlorination step was assigned to the restructuring of the crystal lattice to reach a certain steady state. To avoid this jump in the intra level peak ratio during a MOC experiment it was important to do 2 hours of oxychlorination prior to an experiment.

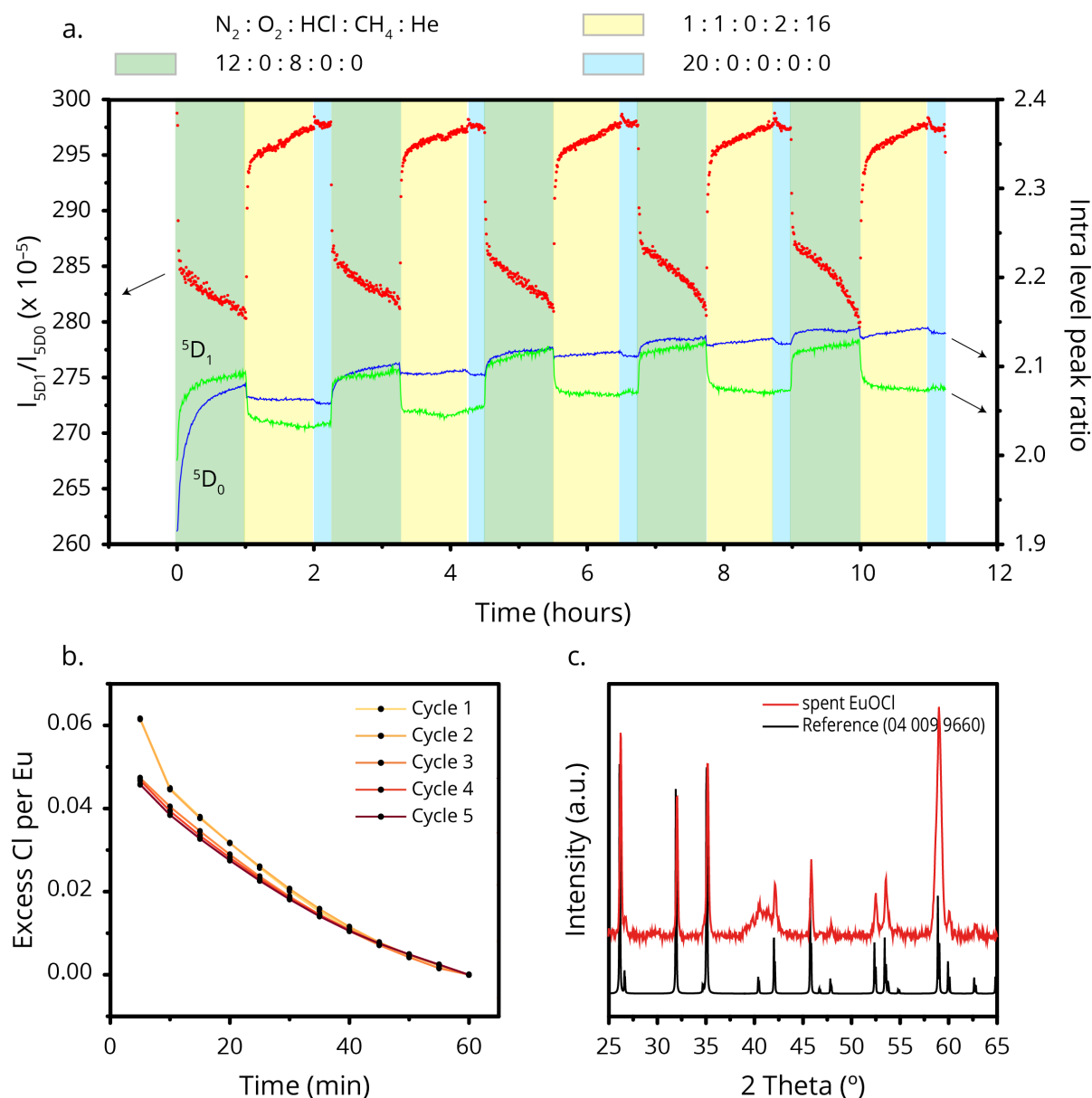


Figure 23. Five chlorination (green) and dechlorination (yellow) cycles were performed at 475 °C (a) luminescence I^{5D_1}/I^{5D_0} ratio and intra level peak ratios versus time on stream. A quick increase in the intra level peak ratios is visible during the first chlorination step, in consecutive cycles the intra level peak ratios increase in a stair-like manner. The quick increase was assigned to the restructuring of the crystal lattice to reach a steady state. The stair-like increase shows that chlorination at 475 °C is still irreversible but has been significantly reduced compared to chlorination at 350 °C. (b) The excess chlorine per europium was calculated from the formed products measured with the GC and is plotted versus the dechlorination time for each cycle. At the start of the first dechlorination cycle the excess chlorine per europium is higher than during the consecutive cycles this coincides with the jump in the intra level peak ratios in a. Between the following cycles the difference in the excess Cl is only small similar to the change in the intra level peak ratios. The state of the catalyst thus changed during the first chlorination step, due to restructuring of the crystal lattice, and remained relatively stable during the consecutive steps. (c) XRD pattern of the spent catalyst together with a EuOCl reference pattern. The XRD pattern of the spent catalyst matches the reference pattern showing that the state of the catalyst indeed did not change drastically during the five chlorination - dechlorination cycles.

The stair-like increase in the intra level peak ratio shows the irreversibility of the catalyst chlorination. Although, chlorination was still irreversible at 475 °C, the change in the intra level peak ratio was very small compared to chlorination at 350 °C (Fig. 18b, 19b) and bulk chlorination was drastically reduced. Figure 23b shows the excess chlorine per europium during each dechlorination step. The excess chlorine per europium deviates slightly, at $t = 5\text{min}$, between the first and second dechlorination cycle, however during the following cycles the excess chlorine per europium is almost equal. The deviation between the first and second cycle coincides with the jump in the intra level peak ratio in figure 23a. The state of the catalyst thus changed during the first cycle and remained relatively stable during the consecutive steps. Furthermore, the excess chlorine per europium, at $t = 5\text{min}$, during each step is significantly lower compared to chlorination at 350 °C, 0.06 Cl per europium compared to 0.65 (Fig. 20, 23b). Although, the chlorination time was half of the duration at 475 °C, the difference is significant as the excess Cl decreased ten fold. The relatively little excess Cl per europium during each cycle and the observation that this value is constant during consecutive cycles, show that chlorination was most likely at the surface and bulk chlorination was limited at 475 °C. The XRD pattern of the spent catalyst was used to check if the state of the catalyst had changed during the five chlorination – dechlorination cycles. Figure 23c shows that the XRD pattern of the spent catalyst matches the EuOCl reference pattern and the state of the catalyst did thus not change.

Bulk chlorination of EuOCl is irreversible as particles agglomerated and the luminescence spectrum of the catalyst was affected. Temperature determination was therefore unreliable when the state of the catalyst changed during an experiment. As bulk chlorination is favored at lower temperatures it was suppressed with reaction temperatures of $\geq 475\text{ °C}$. In addition to limiting bulk chlorination, the EuCl_3 signal was almost completely quenched at those reaction temperatures, which was favorable for temperature measurements as changes in the spectra were limited. For reliable temperature measurements under MOC reaction conditions, reaction temperatures of $\geq 475\text{ °C}$ were thus required.

4.4 Temperature measurements during the methane oxychlorination reaction

Now that the requirements for accurate temperature measurements during MOC were defined, the operating conditions under which these requirements are fulfilled could be determined. The first condition was the use of a bigger sieve fraction (212-425 μm) to make sure the reaction occurs homogeneously over the reactor. The second condition was the use of elevated reaction temperatures ($\geq 475\text{ °C}$) to quench the EuCl_3 signal and to avoid the irreversible bulk chlorination of the catalyst. Finally, 2 hours of pre oxychlorination were required for the restructuring of the lattice to reach a steady state prior to the experiment. With these operating conditions the temperature was measured during several MOC experiments. First, the temperature was measured during MOC at slightly different gas feeds to confirm that temperature measurements were indeed possible under these conditions. Then, the effect of the reaction gas concentrations was studied and finally the effect of the cold inflow of reaction gasses was investigated.

The first experiment consisted of four cycles of consecutively flowing inert nitrogen, oxychlorination reaction mixture and no flows. During the different oxychlorination steps the total flow was kept constant, however the concentrations of the reaction mixture were varied. In this experiment the temperature of the catalyst during the inert nitrogen flow step was expected to be equal to the temperature of the oven (475 °C). Figure 24 shows the temperature and the intra level peak ratios versus the time on stream. The temperature was calculated from the measured $I^5\text{D}_1/I^5\text{D}_0$ ratio with a calibration of the spent catalyst. The error bars consist of

a sum of the Poisson error (eq. 13) and the temperature variation from the set point in the oven of 0.1 °C (Fig. S3).

During the nitrogen flow steps (blue) the temperature was approximately 475 °C, which matched the actual temperature of the oven. When the reaction mixture was flowed over the reactor bed the calculated temperature increased with approximately $\sim +6$ °C, depending on the reaction gas mixture concentrations. Temperature changes were a result of reaction heat formed during exothermic reactions, in this case the MOC reaction and methane combustion, and were therefore dependent on the reaction gas mixture and activity of the catalyst. The reactions occurred at the surface of EuOCl and due to the low surface to volume ratio of the catalyst only a small part of the catalyst participated in the reaction. This resulted in small temperature changes of the catalyst due to formed reaction heat. After the oxychlorination step, the gas flows were stopped and the temperature slowly decreased. This slow instead of a fast decrease was assigned to the presence of leftover reaction mixture in the reactor allowing the reaction, and thus the formation of heat, to continue. After 45 minutes of no gas flow the temperature was still slightly higher than during the nitrogen step. This observation can be the result of the cooling of the catalyst during the nitrogen step as the inflow of nitrogen was relatively cold (~ 110 °C) compared to the reaction temperature. This hypothesis will be studied more in depth later on in this study.

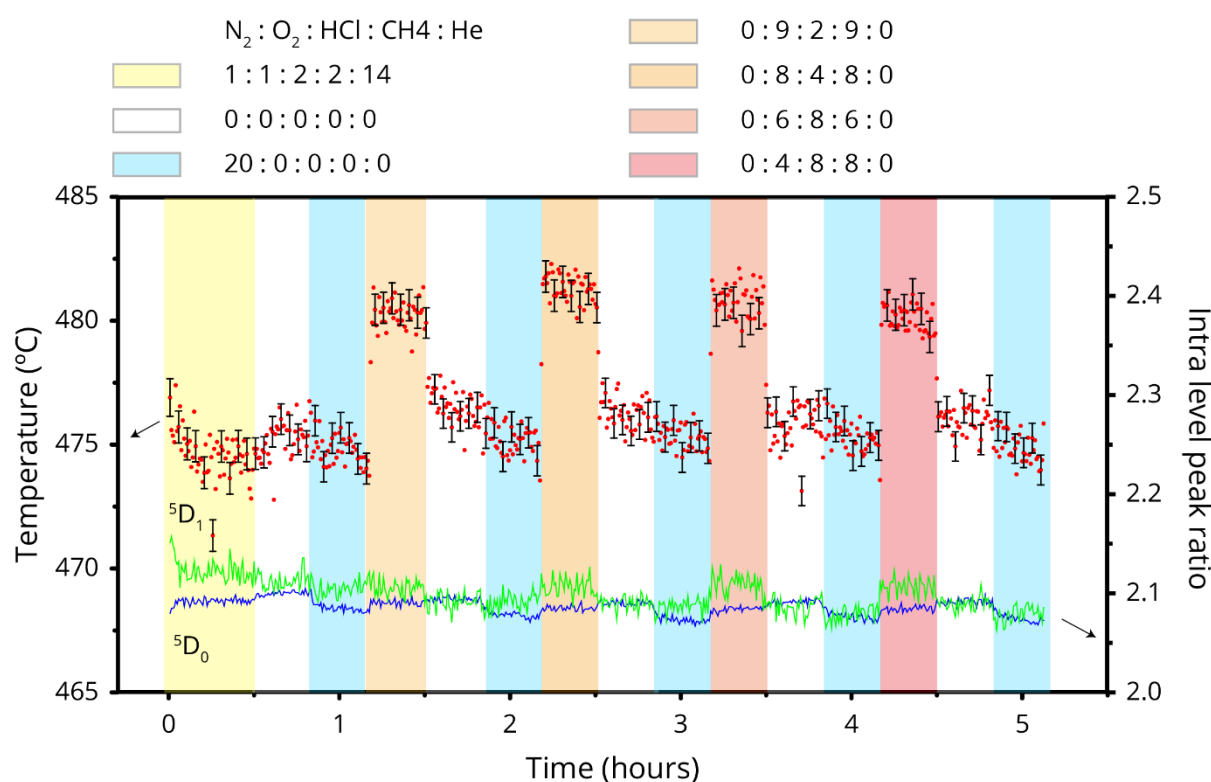


Figure 24. Temperature calculated with the $\hat{F}D_1/\hat{F}D_0$ ratio and intra level peak ratios plotted versus the time on stream. MOC steps were followed by a consecutive no flow and nitrogen flow step. The temperature increased by ~ 5 °C during MOC then slowly cools during the no flow step and cools to 475 °C during the nitrogen flow step. The temperature change during MOC is dependent on the reaction gas mixture. The error bars show the estimated error based on the sum of the Poisson error and the variation in the oven temperature. Temperature measurements were reliable as the intra level peak ratios were constant throughout the experiment.

During the whole experiment the intra level peak ratios were constant, this shows that the state of the catalyst did not change and temperature determination was reliable. The fluctuations in the temperature lie almost completely inside the error bars and therefore the Poisson error and oven variation were a good estimate for the error in the temperature measurements. During this

experiment only one average was used for each measurement due to a weak signal. The error in the measurements would be drastically reduced if the total signal, and thus the number of averages, is increased.

To make sure the calculated temperature changes were indeed a temperature effect, a different type of thermometry was used to verify the results, namely spectral position thermometry. For spectral position thermometry, the 5D_0 peak positioned at $\sim 16150 \text{ cm}^{-1}$ was used. Figure 25 shows the spectral position of this peak over the temperature range $400 - 500 \text{ }^\circ\text{C}$ (red dots). A simple linear fit was used for the calibration (black line). Increasing the temperature from 400 to $500 \text{ }^\circ\text{C}$ resulted in a peak shift to higher energies. Although, the peak shift was small (3 cm^{-1}) a clear trend was visible.

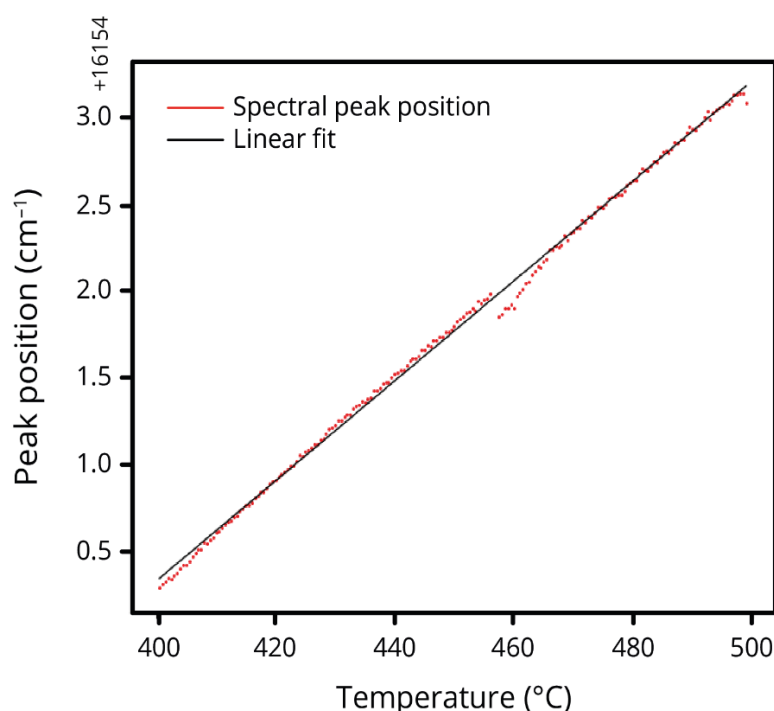


Figure 25. The spectral position of the peak at $\sim 16150 \text{ cm}^{-1}$ plotted versus the temperature in the range $400 - 500 \text{ }^\circ\text{C}$. A simple linear fit (black line) was used for the calibration.

With the calibration for the peak position versus the temperature, the temperature during the MOC experiment was calculated. Figure 26 shows the temperature calculated with band shape thermometry (red dots) and spectral position thermometry (black line). The calculated temperature during MOC ($t = 1.3, 2.3, 3.3, 4.3\text{h}$) was almost equal, while the temperature during the no flow ($t = 0.5, 1.5, 2.5, 3.5, 4.5\text{h}$) and nitrogen ($t = 0.8, 1.8, 2.8, 3.8, 4.8\text{h}$) steps varied slightly between the two methods of temperature determination. This was the result of a not optimized calibration and analysis of the spectral peak position. Furthermore, changes in the peak position were relatively small compared to the resolution of the detector (6 cm^{-1}). Still, the use of different peaks for spectral position thermometry gave similar temperature changes. As temperature measurements via spectral position thermometry were similar to temperature measurements via band shape thermometry the observed temperature changes were confirmed.

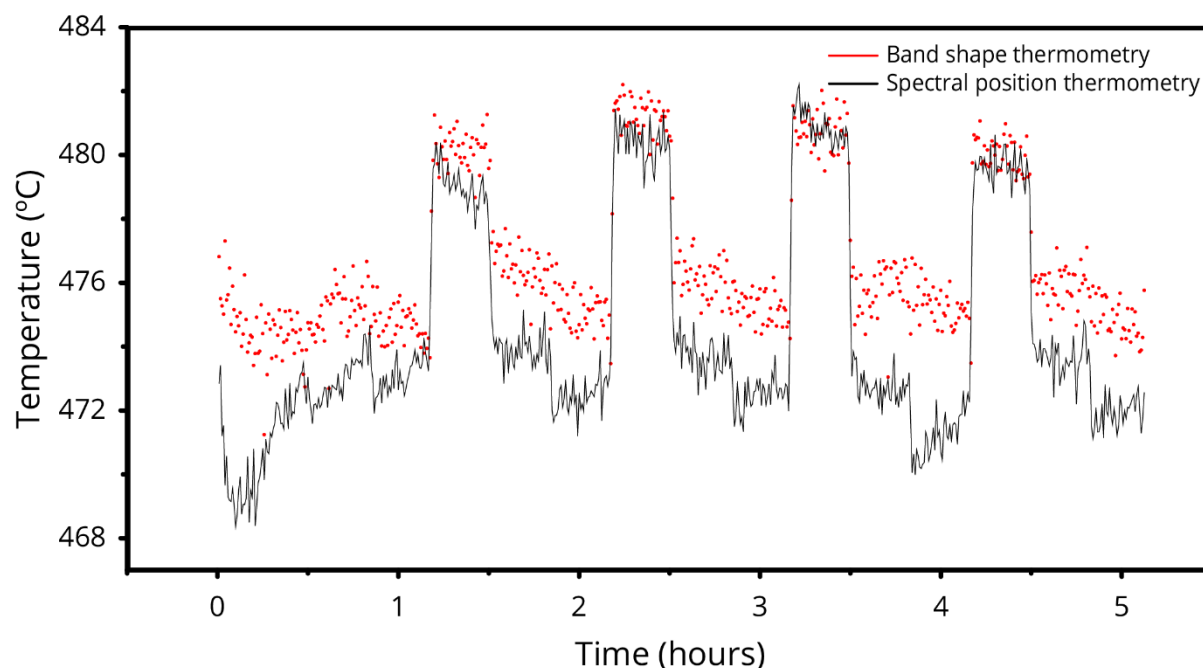


Figure 26. The calculated temperature with band shape thermometry (red dots) and spectral position thermometry (black line) plotted versus the time on stream during the experiment shown in figure 24. The temperature change during MOC calculated with band shape ($\sim +5$ °C) and spectral position thermometry ($\sim +6$ °C) is similar. This verifies that changes measured with bandshape thermometry are indeed a temperature effect.

Now that temperature measurements were reliable during the MOC reaction, EuOCl was used as a thermometer to investigate the effect of the reaction gas concentrations on the local temperature of the catalyst. With the operating conditions as stated priorly, temperature changes were measured during MOC steps with different reaction gasses concentrations, while the total flow (41 ml/min), reaction gas ratio ($O_2 : HCl : CH_4$ of 2 : 1 : 2) and temperature (475 °C) were kept constant. During the experiment the reaction gas concentrations were first increased stepwise and then decreased, using the same concentration steps, to check the reproducibility of the temperature measurements. In between MOC steps either a dechlorination step (1 – 3) or a nitrogen flow step (4 – 7) was performed. The dechlorination step was introduced to limit chlorination of the catalyst in-between MOC steps as there was a leakage of HCl. Figure 27 shows the temperature and the intra level peak ratios versus the time on stream. The error bars represent the estimated error in the measurements introduced by the Poisson error and the temperature variation in the oven.

During the dechlorination step (yellow) the peak ratio, and thus the calculated temperature, increased showing dechlorination of the catalyst. Instead of circumventing chlorination of the catalyst the state of the catalyst thus changed in the opposite direction during the dechlorination step.

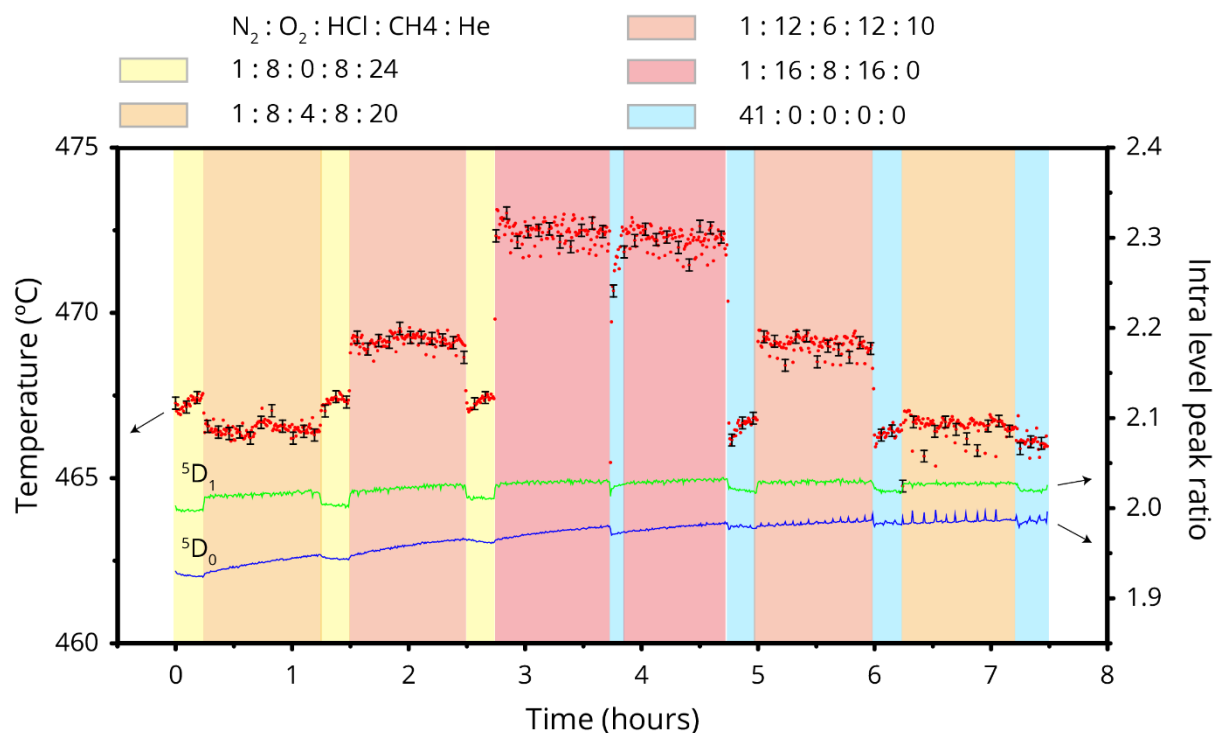


Figure 27. Temperature, calculated with the $\dot{F}D_1/\dot{F}D_0$ ratio, and intra level peak ratios plotted versus the time on stream. The reaction gas concentrations were varied between MOC steps, while the total flow and oven temperature were kept constant. In between MOC steps either a dechlorination step, to circumvent catalyst chlorination due to an HCl leak, or a nitrogen flow step was done. A higher concentration of reaction gasses resulted in more heat formation. Repeating the MOC steps with equal reaction conditions showed equal temperature changes.

Furthermore, if the state of the catalyst had changed during the nitrogen step due to the leakage of HCl, the temperature should have decreased. This was not the case and therefore changes in the state of the catalyst were small under a nitrogen flow at 475 °C. The dechlorination step did thus not have the desired effect and was replaced by a nitrogen flow step.

The temperature during dechlorination and nitrogen flow was expected to be 475 °C, but deviated from this temperature by approximately 8 °C. This observation was assigned to the leakage of HCl, which has a stronger effect at lower temperatures, and problems with the oven ramp as this caused errors in the calibration of the thermometer. The temperature measurements were thus not accurate, but could be used for indicative conclusions. Temperature changes were determined by comparing the temperature of the nitrogen step with the temperature during MOC because the higher calculated temperature during dechlorination was not a temperature effect but an effect of the change in the state of the catalyst.

During the two MOC reaction steps with reaction gasses $N_2 : O_2 : HCl : CH_4 : He$ of 1 : 8 : 4 : 8 : 20 ml/min ($t = 0.25, 6.25$ h) the temperature was equal and slightly higher ($\sim + 0.5$ °C) than during the nitrogen flow steps ($t = 4.75, 6, 7.25$ h). With higher reaction gas concentrations of 1 : 12 : 6 : 12 : 10 ml/min ($t = 1.5, 5$ h) the temperature was also equal during both steps and the temperature change was higher compared to the lower concentration ($\sim + 2.5$ °C). During the highest reaction gas concentration steps of 1 : 16 : 8 : 16 : 0 ml/min ($t = 2.75, 3.85$ h), the temperature change increased to $\sim + 6$ °C. The bigger temperature change was assigned to the formation of more products during MOC with higher reaction gas concentrations and thus more released reaction heat. During the whole experiment the intra level peak ratios only changed slightly and therefore the state of the catalyst did not change significantly. As the state of the catalyst did not change much and the temperature changes during MOC were equal for the identical reaction steps, the temperature measurements were reproducible.

The error bars in figure 27 covered most of the measurements, except for the highest reaction gas concentration steps, and were significantly narrower than during the previous experiment (Fig. 24). A new laser window was used during this experiment, which increased the signal and reduced the Poisson error drastically compared to the previous experiment. However, the new window also introduced a background signal that needed to be corrected for. The error caused by this background was more significant for the higher concentration measurements due to the worse signal to noise ratio at the higher temperature. The error in the temperature was significantly reduced with the new laser window however the correction for its background signal needs to be optimized.

In the first experiment (Fig. 24) a temperature difference between the no flow and nitrogen step was visible. When the nitrogen flow was switched on after 45 minutes of no flow the temperature decreased. This temperature change could not be assigned to reaction heat as all the left-over reaction mixture in the reactor was expected to have reacted at this point. The temperature change could therefore be a result of the cooling of the catalyst by the cold inert gas inflow (110 °C). As there was still a leakage of HCl, the cooling effect of the gasses, was measured during oxychlorination to keep the state of the catalyst stable. Constant O₂ : HCl : CH₄ flows of 8 : 4 : 8 ml/min and a constant reaction temperature of 475 °C were used, while the helium flow was varied to qualitatively measure the effect of the cold gas inflow on the catalyst temperature. Helium was used instead of nitrogen, because its higher specific heat capacity (Table 1) was expected to have a stronger effect on the catalyst temperature. Also, during MOC usually the helium flow was changed instead of the intern standard nitrogen, which made helium the better choice as variable for this experiment.

Table 1. Specific heat capacity of the gasses used in the MOC experiments.

Specific heat capacity	Nitrogen	Oxygen	Methane	HCl	Helium
Constant volume (kJkg ⁻¹ K ⁻¹)	1.04	0.919	2.22	0.795	5.19
Constant pressure (kJkg ⁻¹ K ⁻¹)	0.743	0.659	1.7	0.567	3.12

Figure 28 shows the temperature and the intra level peak ratios versus the time on stream. The temperature during the nitrogen flow step (blue) still deviates from the reaction temperature of 475 °C. Furthermore, due to the HCl leak constant flows of MOC reaction gasses were used during the experiment. Dilution of the reaction gas mixture with helium results in a lower residence time in the reactor, which is expected to reduce the amount of formed products and thus less reaction heat. Therefore temperature changes during the different MOC steps due to reaction heat were not constant and quantitative results on the temperature changes during the different MOC steps were inhibited.

When the MOC reaction gas mixture was not diluted with helium (t = 0.1, 1.3h) the temperature change was approximately + 3 °C. When the reaction gas mixture was diluted with 21 ml/min helium (t = 2.6h) the temperature change decreased to approximately – 0.5 °C. Further dilution of the reaction gas mixture with 41 ml/min helium (t = 3.85h) resulted in a more negative temperature change of ~-2 °C. These negative temperature changes could not be the result of the exothermic reaction and were therefore the result of the cooling of the catalyst by the cold flow of helium.

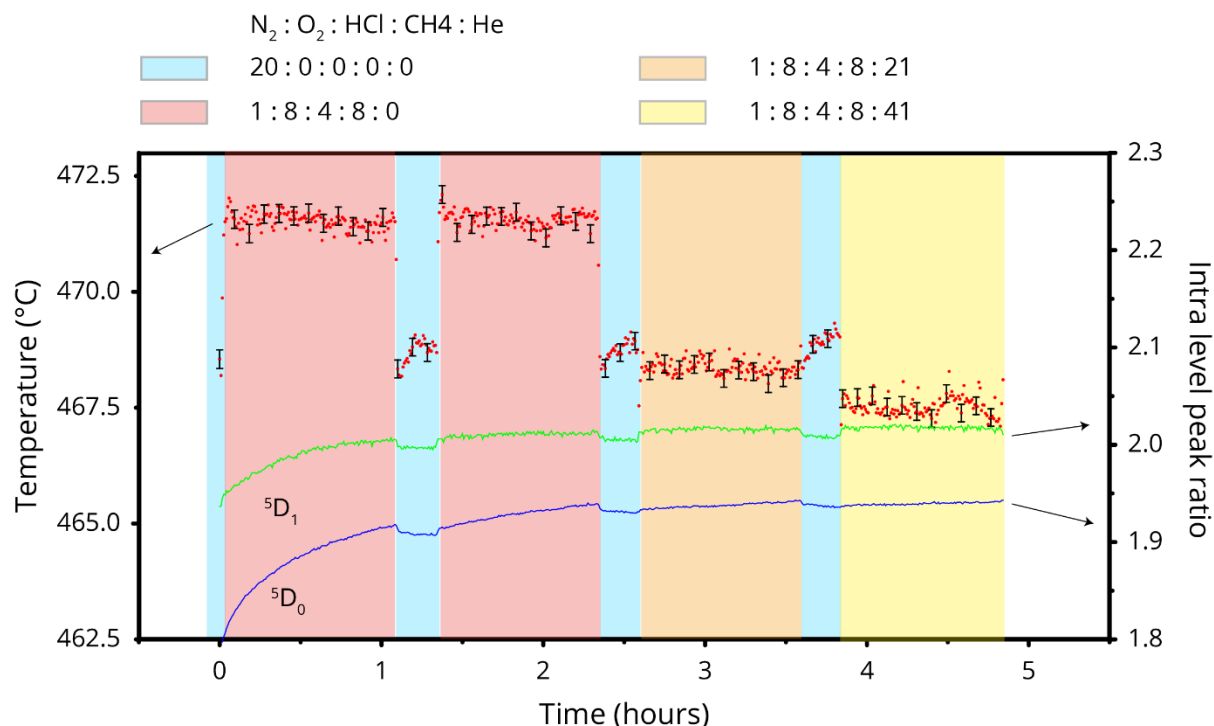


Figure 28. Temperature, calculated with the I^5D_1/I^5D_0 ratio, and intra level peak ratios plotted versus the time on stream. The reaction gas flows were kept constant during the experiment, while the helium flow was changed. Nitrogen was flushed in between MOC steps. Without dilution of the reaction gas with helium the temperature increased by $\sim +3$ °C. Upon dilution with helium the temperature change became negative. The intra level peak ratios do not change when the flows are changed. The negative temperature change can thus not be the result of the exothermic MOC reaction and was assigned to the cooling of the catalyst by the cold inflow of reaction gasses.

The catalyst was thus cooled by the cold inflow of gasses during all experiments. Prior temperature calibrations were made under a nitrogen flow and the catalyst was therefore cooled during calibrations. Although, compared to helium the temperature change during those calibrations was smaller due to the lower specific heat capacity of nitrogen, there was a systematic error in all calibrations and therefore also in the temperature measurements. An estimated guess for this error was made based on the temperature difference between the no flow and nitrogen step flow in figure 24. This error was approximately $+1$ °C for all calculated temperatures and was dependent on the flows. This error did not affect calculated temperature changes, it did however affect the absolute temperatures.

With the established boundary conditions required for reliable temperature measurements under MOC reaction conditions, the temperature was monitored during several MOC experiments. Temperature measurements with those boundary conditions were reliable and could accurately determine temperature changes of the catalyst. Temperature changes were proportional to the concentrations of reaction gasses. It was expected that the formation of more reaction products resulted in more reaction heat. Temperature measurements were reproducible and the error in measurements was estimated well with the sum of the Poisson error and the variation in the oven. It was found that the cold inflow of reaction gasses resulted in the cooling of catalyst bodies and thus a systematic error of approximately $+1$ °C was introduced in all measurements.

5 CONCLUSION

We have used band shape thermometry to monitor the local temperature of our EuOCl catalyst during the MOC reaction. With the luminescence intensity ratio of the two thermally coupled states of europium the temperature, calculated with the I^5D_1/I^5D_0 ratio, was measured accurately under inert environment. In order to obtain a representative spectrum independent of the measured location in the reactor under MOC reaction conditions, a big catalyst sieve fraction (212-425 μm) and high flows (60 ml/min, 20% HCl) were used during chlorination of the catalyst. Catalyst chlorination resulted in a drastic decrease of the I^5D_1/I^5D_0 ratio and thereby introduced a significant error to temperature measurements. Additionally, TEM images of the chlorinated catalyst showed particle agglomeration. As temperature measurements are only reliable when the state of the catalyst is stable, bulk chlorination needed to be circumvented. The intra level peak ratios were introduced, as a measure for the degree of chlorination of the catalyst, to detect when changes in the I^5D_1/I^5D_0 ratio are due to catalyst chlorination instead of a temperature effect. Chlorination of the catalyst was favored at lower temperatures and could thus be suppressed at temperatures ≥ 475 °C. At these elevated temperatures the EuCl_3 luminescence signal was fully quenched, and temperature determination was possible. Furthermore, to ensure a stable state of the catalyst during temperature measurements, 2 hours of pre oxychlorination was done prior to experiments to enable restructuring of the crystal lattice.

With the operating conditions required for temperature determination under reaction conditions, MOC experiments were performed to study the temperature effects of several parameters during the reaction. Temperature changes of ~ 5 °C were observed when a reaction gas mixture of $\text{N}_2 : \text{O}_2 : \text{HCl} : \text{CH}_4 : \text{He}$ of 0 : 8 : 4 : 8 : 0 ml/min was used. Temperature measurements were accurate and reliable as the calculated and measured temperature under nitrogen were equal and the state of the catalyst was stable. The relatively small temperature change was assigned to the low surface to volume ratio of our catalyst. It was shown that the temperature change during MOC was proportional to the reaction gas mixture concentrations. This can be the result of increased product formation and thus more heat formation. Temperature changes were reproducible as repeating the use of the different concentrations resulted in equal temperature changes. Furthermore, it was observed that upon dilution of the reaction gas feed with helium, the temperature change was negative. A negative temperature change could not be a result of the exothermic MOC reaction and was therefore assigned to the cooling of the catalyst bodies by the cold inflow (110 °C) of gasses. All prior calibrations were performed under a nitrogen flow and therefore a systematic error was introduced in all temperature measurements. This error was estimated, based on the temperature difference between the nitrogen flow and no flow, and is approximately +1 °C. This error did not affect the temperature changes it did however affect the absolute calculated temperature.

Concluding, we were able to determine the temperature during the MOC reaction accurately using our EuOCl catalyst as a thermometer. Temperature changes between 0.5 – 6 °C were measured. A temperature change of approximately +5 °C can have a significant effect on the activity and selectivity of the reaction, the risk of thermal runaway is low during our experiments as the temperature was constant throughout MOC. The ability to measure the temperature locally on the active site enables investigation of the mechanisms behind the promising catalytic results of EuOCl for the MOC reaction. Additionally, if the MOC over EuOCl would be commercialized an additional thermometer would be unnecessary as the catalyst could be used for monitoring of the temperature.

6 OUTLOOK

The promising results published in this study are a good basis for further research. However, fine tuning of the conditions and experimental setups are necessary to increase the accuracy of temperature determination further. First of all, the set up can be improved. Currently, the laser seems contaminated as a signal is measured in an empty oven. This requires another fitting step, which can introduce an error into temperature determination. Also, gas flows should be heated prior to entering the reactor to minimize their effect on the temperature or the temperature should be corrected for the used flows with their respective temperatures and specific heat capacities. Adding additional lasers on top of each other would allow for simultaneous measurements of all heights in the reactor. This would be very interesting to study thermodynamics over the reactor, especially when combined with a model describing reaction heat release and heat transfer. Linking product formation to the temperature changes, the use of differently shaped reactors and the use of well defined particle sizes could help in this regard. The use of supported catalyst particles would offer many opportunities as temperature changes would be expected to be much bigger. The Raman laser has a certain penetration depth and therefore current measurements give an average of mostly bulk and some surface EuOCl . Heat transfer to the bulk takes time and is an additional process that should be accounted for in the model. Increasing the surface to volume ratio by using supported particles would solve this issue plus it would enable investigation of the active site on a much smaller scale. However, in previous measurements of europium supported on zirconia or silica the signal of the europium was too little compared to the support and therefore temperature determination was impossible. So, finding a suitable europium concentration and support would be a challenge. Another possibility would be to change excitation wavelengths of the Raman laser to vary the penetration depth of the laser as lower excitation wavelengths result in a lower penetration depth.⁵⁴ However, doing so results in excitations into higher energy levels, which in turn results in additional processes such as luminescence quenching.

Furthermore, our thermometer currently needs a calibration at the end of an experiment to calculate temperatures during the experiment. Therefore, the thermometer is not yet suitable for real time monitoring of the temperature, but for research purposes only. If a calibration can be made for a steady state of the catalyst that is useful for future experiments the python script could be changed to measure temperatures on the spot. To do so it might be useful to use different concentrations of reactants and make multiple calibrations. Each calibration can then be used for future experiments that use those concentrations.

ACKNOWLEDGMENT

I would like to thank Bas Terlingen for the help throughout the whole project; Freddy Rabouw for his helpful criticism during our repetitive meetings; Bert Weckhuysen for the possibility of doing research in the Advanced Research Center for Chemical Building Blocks (ARC CBBC); Eline Hutter for her help during the early phase of the project; and Thomas van Swieten for his assistance with the luminescence lifetimes measurements.

LITERATURE LIST:

- (1) Zichittella, G.; Paunović, V.; Amrute, A. P.; Pérez-Ramírez, J. Catalytic Oxychlorination versus Oxybromination for Methane Functionalization. *ACS Catal.* **2017**, *7*, 1805–1817. <https://doi.org/10.1021/acscatal.6b03600>.
- (2) Horn, R.; Schlögl, R. Methane Activation by Heterogeneous Catalysis. *Catal. Letters* **2015**, *145* (1), 23–39. <https://doi.org/10.1007/s10562-014-1417-z>.
- (3) Peringer, E.; Podkolzin, S. G.; Jones, M. E.; Olindo, R.; Lercher, J. A. LaCl₃-Based Catalysts for Oxidative Chlorination of CH₄. *Top. Catal.* **2006**, *38* (1–3), 211–220. <https://doi.org/10.1007/s11244-006-0085-7>.
- (4) Zhidomirov, G. M.; Avdeev, V. I.; Zhanpeisov, N. U.; Zakharov, I. I.; Yudanov, I. V. Molecular Models of Active Sites of C1 and C2 Hydrocarbon Activation. *Catal. Today* **1995**, *24* (3), 383–387. [https://doi.org/10.1016/0920-5861\(95\)00063-L](https://doi.org/10.1016/0920-5861(95)00063-L).
- (5) Terlingen, B. J. P.; Oord, R.; Ahr, M. P.; Hutter, E. M.; Lare, C. E. J. Van; Bert, M. Mechanistic Insights in the Lanthanide-Catalyzed Oxychlorination of Methane as Revealed by Operando Spectroscopy. **2021**.
- (6) Onukwulia, O. D.; Omotioma, M. Study of Bitter Leaves Extract as Inhibitive Agent in HCL Medium for the Treatment of Mild Steel through Pickling. *Port. Electrochim. Acta* **2019**, *37* (2), 115–121. <https://doi.org/10.4152/pea.201902115>.
- (7) Hermansson, A. W.; Syafie, S. Model Predictive Control of PH Neutralization Processes: A Review. *Control Eng. Pract.* **2015**, *45*, 98–109. <https://doi.org/10.1016/j.conengprac.2015.09.005>.
- (8) Monteagudo, J. M.; Ortiz, M. J. Removal of Inorganic Mercury from Mine Waste Water by Ion Exchange. *J. Chem. Technol. Biotechnol.* **2000**, *75* (9), 767–772. [https://doi.org/10.1002/1097-4660\(200009\)75:9<767::AID-JCTB281>3.0.CO;2-1](https://doi.org/10.1002/1097-4660(200009)75:9<767::AID-JCTB281>3.0.CO;2-1).
- (9) Gorguner, M.; Aslan, S.; Inandi, T.; Cakir, Z. Reactive Airways Dysfunction Syndrome in Housewives Due to A Bleach-Hydrochloric Acid Mixture. *Inhal. Toxicol.* **2004**, *16* (2), 87–91. <https://doi.org/10.1080/08958370490265004>.
- (10) Singha, A.; Quraishi, M. A. Acidizing Corrosion Inhibitors: A Review. *J. Mater. Environ. Sci.* **2015**, *6* (1), 224–235.
- (11) S., A.; A., G. *Ullmann's Encyclopedia of Industrial Chemistry Hydrochloric Acid*; 2000.
- (12) Pérez-Ramírez, J.; Mondelli, C.; Schmidt, T.; Schlüter, O. F. K.; Wolf, A.; Mleczko, L.; Dreier, T. Sustainable Chlorine Recycling via Catalysed HCl Oxidation: From Fundamentals to Implementation. *Energy Environ. Sci.* **2011**, *4* (12), 4786–4799. <https://doi.org/10.1039/c1ee02190g>.
- (13) Muchortova, L. I.; Konstantinova, T. G. Disposal of Waste Hydrochloric Acid in Chloromethane Production. *Int. Res. J.* **2017**, *4* (58), 78–79.
- (14) López, N.; Gómez-Segura, J.; Marín, R. P.; Pérez-Ramírez, J. Mechanism of HCl Oxidation (Deacon Process) over RuO₂. *J. Catal.* **2008**, *255* (1), 29–39. <https://doi.org/10.1016/j.jcat.2008.01.020>.
- (15) Ohtsuka, Y.; Tamai, Y. Oxychlorination of Methane in the Presence of Molten Metallic Chlorides. *J. Catal.* **1978**, *51* (2), 169–172. [https://doi.org/10.1016/0021-9517\(78\)90290-7](https://doi.org/10.1016/0021-9517(78)90290-7).
- (16) Hur, E.; Kim, D. H. Effect of Reactant Ratios on Methane Oxychlorination Over CeO₂ Catalyst. *J. Nanosci. Nanotechnol.* **2019**, *19* (9), 5961–5964. <https://doi.org/10.1166/jnn.2019.16565>.
- (17) Garcia, C. L.; Resasco, D. E. Effects of the Support and the Addition of a Second Promoter on Potassium Chloride-Copper(II) Chloride Catalysts Used in the Oxychlorination of Methane. *Appl. Catal.* **1989**, *46* (2), 251–267. [https://doi.org/10.1016/S0166-9834\(00\)81121-5](https://doi.org/10.1016/S0166-9834(00)81121-5).

- (18) Kim, J.; Ryou, Y.; Hwang, G.; Bang, J.; Jung, J.; Bang, Y.; Kim, D. H. Oxychlorination of Methane over FeOx/CeO₂ Catalysts. *Korean J. Chem. Eng.* **2018**, *35* (11), 2185–2190. <https://doi.org/10.1007/s11814-018-0135-4>.
- (19) Chemistry, E.; Chemistry, C. Oxychlorination of Methane To Methyl Chloride At 300 ~. **1995**, *31* (1), 29–33.
- (20) Peringer, E.; Salzinger, M.; Hutt, M.; Lemonidou, A. A.; Lercher, J. A. Modified Lanthanum Catalysts for Oxidative Chlorination of Methane. *Top. Catal.* **2009**, *52* (9), 1220–1231. <https://doi.org/10.1007/s11244-009-9265-6>.
- (21) Podkolzin, S. G.; Stangland, E. E.; Jones, M. E.; Peringer, E.; Lercher, J. A. Methyl Chloride Production from Methane over Lanthanum-Based Catalysts. *J. Am. Chem. Soc.* **2007**, *129* (9), 2569–2576. <https://doi.org/10.1021/ja066913w>.
- (22) Van Der Heijden, A. W. A. M.; Ramos, M. G.; Weckhuysen, B. M. Intermediates in the Destruction of Chlorinated C₁ Hydrocarbons on La-Based Materials: Mechanistic Implications. *Chem. - A Eur. J.* **2007**, *13* (34), 9561–9571. <https://doi.org/10.1002/chem.200700901>.
- (23) Health and Safety Executive. Chemical Reaction Hazards and the Risk of Thermal Runaway. *Www.Hse.Gov.Uk* **2014**, 1–6.
- (24) Hou, J.; Lu, L.; Wang, L.; Ohma, A.; Ren, D.; Feng, X.; Li, Y.; Li, Y.; Ootani, I.; Han, X.; Ren, W.; He, X.; Nitta, Y.; Ouyang, M. Thermal Runaway of Lithium-Ion Batteries Employing LiN(SO₂F)₂-Based Concentrated Electrolytes. *Nat. Commun.* **2020**, *11* (1), 1–11. <https://doi.org/10.1038/s41467-020-18868-w>.
- (25) Geitenbeek, R. G.; Nieuwelink, A. E.; Jacobs, T. S.; Salzmann, B. B. V.; Goetze, J.; Meijerink, A.; Weckhuysen, B. M. In Situ Luminescence Thermometry to Locally Measure Temperature Gradients during Catalytic Reactions. *ACS Catal.* **2018**, *8* (3), 2397–2401. <https://doi.org/10.1021/acscatal.7b04154>.
- (26) Geitenbeek, R. G. *Luminescence Thermometry: Fundamentals and Applications*; 2018.
- (27) Jaque, D.; Vetrone, F. Luminescence Nanothermometry. *Nanoscale* **2012**, *4* (15), 4301–4326. <https://doi.org/10.1039/c2nr30764b>.
- (28) Dai, Q.; Zhang, Y.; Wang, Y.; Hu, M. Z.; Zou, B.; Wang, Y.; Yu, W. W. Size-Dependent Temperature Effects on PbSe Nanocrystals. *Langmuir* **2010**, *26* (13), 11435–11440. <https://doi.org/10.1021/la101545w>.
- (29) Kolesnikov, I. E.; Mamonova, D. V.; Kurochkin, M. A.; Kolesnikov, E. Y.; Lähderanta, E. Multimode Luminescence Thermometry Based on Emission and Excitation Spectra. *J. Lumin.* **2021**, *231* (November 2020), 1–6. <https://doi.org/10.1016/j.jlumin.2020.117828>.
- (30) Lojpur, V.; Nikolić, M. G.; Jovanović, D.; Medić, M.; Antić, Ž.; Dramićanin, M. D. Luminescence Thermometry with Zn₂SiO₄:Mn²⁺ Powder. *Appl. Phys. Lett.* **2013**, *103* (14), 2–5. <https://doi.org/10.1063/1.4824208>.
- (31) Geitenbeek, R. G.; Vollenbroek, J. C.; Weijgertze, H. M. H.; Tregouet, C. B. M.; Nieuwelink, A. E.; Kennedy, C. L.; Weckhuysen, B. M.; Lohse, D.; Van Blaaderen, A.; Van Den Berg, A.; Odijk, M.; Meijerink, A. Luminescence Thermometry for: In Situ Temperature Measurements in Microfluidic Devices. *Lab Chip* **2019**, *19* (7), 1236–1246. <https://doi.org/10.1039/c8lc01292j>.
- (32) Peng, H.; Song, H.; Chen, B.; Wang, J.; Lu, S.; Kong, X.; Zhang, J. Temperature Dependence of Luminescent Spectra and Dynamics in Nanocrystalline Y₂O₃:Eu³⁺. *J. Chem. Phys.* **2003**, *118* (7), 3277–3282. <https://doi.org/10.1063/1.1538181>.
- (33) Wang, X.; Zheng, J.; Xuan, Y.; Yan, X. Optical Temperature Sensing of NaYbF₄:Tm³⁺@SiO₂ Core-Shell Micro-Particles Induced by Infrared Excitation. *Opt. Express* **2013**, *21* (18), 21596. <https://doi.org/10.1364/oe.21.021596>.
- (34) Wang, S.; Westcott, S.; Chen, W. Nanoparticle Luminescence Thermometry. *J. Phys.*

- Chem. B* **2002**, *106* (43), 11203–11209. <https://doi.org/10.1021/jp026445m>.
- (35) Wiedemann, E. “Über Fluoreszenz Und Phosphoreszenz, I. Abhandlung” (On Fluorescence and Phosphorescence). *Ann. Phys.* **1888**, *34*, 446–463.
- (36) Murthy, K. V. R.; Virk, H. S. Luminescence Phenomena: An Introduction. *Defect Diffus. Forum* **2014**, *347*, 1–34. <https://doi.org/10.4028/www.scientific.net/DDF.347.1>.
- (37) Binnemans, K. Lanthanide-Based Luminescent Hybrid Materials. *Chem. Rev.* **2009**, *109* (9), 4283–4374. <https://doi.org/10.1021/cr8003983>.
- (38) Walsh, B. M. Judd-Ofelt Theory: Principles and Practices Brian m. Walsh. *Adv. Spectrosc. Lasers Sens.* **2006**, 403–433.
- (39) Winkler, R. *Spin–Orbit Coupling Effects in Two-Dimensional Electron and Hole Systems*; Springer US, 2003. <https://doi.org/10.1787/9789264059597-8-en>.
- (40) Dieke, G. H.; Satten, R. A. Spectra and Energy Levels of Rare Earth Ions in Crystals. *Am. J. Phys.* **1970**, *38* (3), 399–400. <https://doi.org/10.1119/1.1976350>.
- (41) Luís Dias Carlos, Fernando Palacio, F. P. P. Thermometry at the Nanoscale: Techniques and Selected Applications.
- (42) Rabouw, F. *Poisson Statistics and the Gaussian Approximation*; 2021; pp 1–5.
- (43) Dramićanin, M. D. Sensing Temperature via Downshifting Emissions of Lanthanide-Doped Metal Oxides and Salts. A Review. *Methods Appl. Fluoresc.* **2016**, *4* (4). <https://doi.org/10.1088/2050-6120/4/4/042001>.
- (44) Blasse, G. The Influence of Charge-Transfer and Rydberg States on the Luminescence Properties of Lanthanides and Actinides. *Spectra Chem. Interact.* **2007**, No. 112, 43–79. <https://doi.org/10.1007/bfb0116577>.
- (45) Blasse, G.; Bril, A. Photoluminescent Efficiency of Phosphors with Electronic Transitions in Localized Centers. *J. Electrochem. Soc.* **1968**, *115* (10), 1067. <https://doi.org/10.1149/1.2410880>.
- (46) Fonger, W. H.; Struck, C. W. Eu³⁺ Resonance Quenching to the Charge-Transfer States in Y₂O₂S, La₂O₂S, and LaOCl. *J. Chem. Phys.* **1970**, *52* (12), 6364–6372. <https://doi.org/10.1063/1.1672952>.
- (47) Weber, M. J. Radiative and Multiphonon Relaxation of Rare-Earth Ions in Y₂O₃. *Phys. Rev.* **1968**, *171* (2), 1–8.
- (48) Gao, G.; Turshatov, A.; Howard, I. A.; Busko, D.; Joseph, R.; Hudry, D.; Richards, B. S. Up-Conversion Fluorescent Labels for Plastic Recycling: A Review. *Adv. Sustain. Syst.* **2017**, *1* (5). <https://doi.org/10.1002/advsu.201600033>.
- (49) Maity, A.; Jana, S.; Ghosh, S.; Sharma, S. Spectroscopic Investigation on Europium (Eu³⁺) Doped Strontium Zinc Lead Phosphate Glasses with Varied ZnO and PbO Compositions. *J. Non. Cryst. Solids* **2020**, *550* (June), 120322. <https://doi.org/10.1016/j.jnoncrysol.2020.120322>.
- (50) Blasse, G. On the Eu³⁺ Fluorescence of Mixed Metal Oxides. IV. The Photoluminescent Efficiency of Eu³⁺-Activated Oxides. *J. Chem. Phys.* **1966**, *45* (7), 2356–2360. <https://doi.org/10.1063/1.1727946>.
- (51) Dexter, D. L. A Theory of Sensitized Luminescence in Solids. *J. Chem. Phys.* **1953**, *21* (5), 836–850. <https://doi.org/10.1063/1.1699044>.
- (52) Peringer, E.; Tejuja, C.; Salzinger, M.; Lemonidou, A. A.; Lercher, J. A. On the Synthesis of LaCl₃ Catalysts for Oxidative Chlorination of Methane. *Appl. Catal. A Gen.* **2008**, *350* (2), 178–185. <https://doi.org/10.1016/j.apcata.2008.08.009>.
- (53) Hölsä, J.; Porcher, P. Free Ion and Crystal Field Parameters for REOCl:Eu³⁺. *J. Chem. Phys.* **1981**, *75* (5), 2108–2117. <https://doi.org/10.1063/1.442314>.
- (54) Song, J.; Yang, C.; Hu, H.; Dai, X.; Wang, C.; Zhang, H. Penetration Depth at Various Raman Excitation Wavelengths and Stress Model for Raman Spectrum in Biaxially-

- Strained Si. *Sci. China Physics, Mech. Astron.* **2013**, *56* (11), 2065–2070. <https://doi.org/10.1007/s11433-013-5205-3>.
- (55) Mooney, J.; Kambhampati, P. Get the Basics Right: Jacobian Conversion of Wavelength and Energy Scales for Quantitative Analysis of Emission Spectra. *J. Phys. Chem. Lett.* **2013**, *4* (19), 3316–3318. <https://doi.org/10.1021/jz401508t>.
- (56) Meier, R. J. On Art and Science in Curve-Fitting Vibrational Spectra. *Vib. Spectrosc.* **2005**, *39* (2), 266–269. <https://doi.org/10.1016/j.vibspec.2005.03.003>.

SUPPORTING INFORMATION:

S1. Energy levels EuOCl

Table 2. Energy values of the range of interest for EuOCl

			ΔE			
$^5D^1$	E	19060	1781			
	A2	18985	1706			
$^5D^0$	A1	17279				
				$^5D_1 - E$	$^5D_1 - A2$	5D_0
			ΔE	ΔE	ΔE	
$^7F^4$	B''	3060	16000	15925	14219	
	B'	3027	16033	15958	14252	
	E	3016	16044	15969	14263	
	A1	3004	16056	15981	14275	
	E	2912	16148	16073	14367	
	A2	2867	16193	16118	14412	
	A1	2713	16347	16272	14566	
$^7F^3$	B'	2075	16985	16910	15204	
	B''	2010	17050	16975	15269	
	E	2004	17056	16981	15275	
	E	1902	17158	17083	15377	
	A2	1886	17174	17099	15393	
$^7F^2$	B'	1376	17684	17609	15903	
	A1	1106	17954	17879	16173	
	E	1025	18035	17960	16254	
	B''	997	18063	17988	16282	
$^7F^1$	E	479	18581	18506	16800	
	A2	189	18871	18796	17090	
$^7F^0$	A1	0	19060	18985	17279	

S2. Data analysis

Energy conversion

Before the fit, the x-axis is converted from nm to cm^{-1} as using the energy scale gives a better representation of the data especially for quantitative analysis such as nano thermometry. However, the inverse relationship between the two presents a challenge and has previously resulted in incorrect conclusions. Converting the wavelength to the energy scale proceeds via (eq. 20):⁵⁵

$$E = \frac{hc}{\lambda} \quad [20]$$

Although, the mere conversion of the x-values may seem sufficient to convert the x-axis this is incorrect. Note that counts recorded by a spectrometer are really signal per unit wavelength or signal per unit energy. Because there is an inverse relationship between the two quantities, the intervals in the wavelength spectrum, $d\lambda$, are not equally spaced on the energy spectrum. Considering the counts as some function $f(\lambda)$ and conservation of energy, then (eq. 21):⁵⁵

$$f(E)dE = f(\lambda)d\lambda \quad [21]$$

Combining the two equations gives (eq. 22):

$$f(E) = f(\lambda) \frac{d\lambda}{dE} = f(\lambda) \frac{d}{dE} \left(\frac{hc}{E} \right) = -f(\lambda) \frac{hc}{E^2} \quad [22]$$

The minus sign merely represents the different directions of integration and can thus be ignored. Equation 22 is called the Jacobian transformation and it should be used to scale all counts in addition to the scaling of the x-axis by equation 20.

Peak fitting and deconvolution

Important for peak fitting and deconvolution is to use the proper procedure as errors could lead to inaccuracy in the determination of the temperature. Although, curve fitting is a procedure that is often used and thus expected to be well-known, it is not uncommon that the procedure is done in an inappropriate, i.e. scientific unjustifiable, way. Often a Gauss-Lorentz sum function is used for fitting peaks with the form:⁵⁶

$$S(\nu) = \alpha G(\nu) + (1 - \alpha)L(\nu) \quad [23]$$

This is incorrect as most profiles are intrinsically Lorentzian in shape. This means that the line profile originating from the physical interactions is Lorentzian in shape and thus not considering the effects of for example the spectrometer. Although, the intrinsic line shapes are Lorentzian, instrumental effects may cause gaussian line broadening resulting in a Voigt profile, which implies that the Lorentzian profile is multiplied by the Gaussian profile. This would thus be a multiplication and not a sum of the Gaussian and Lorentzian profile as function 23 states, the sum function thus has no physical basis and its use is incorrect.⁵⁶ Europium is characterized by its sharp peaks and using an only Lorentzian profile for the fit of the ${}^5\text{D}_0$ region, 16500 to 15500 cm^{-1} , results in a good fit (Fig. 29).

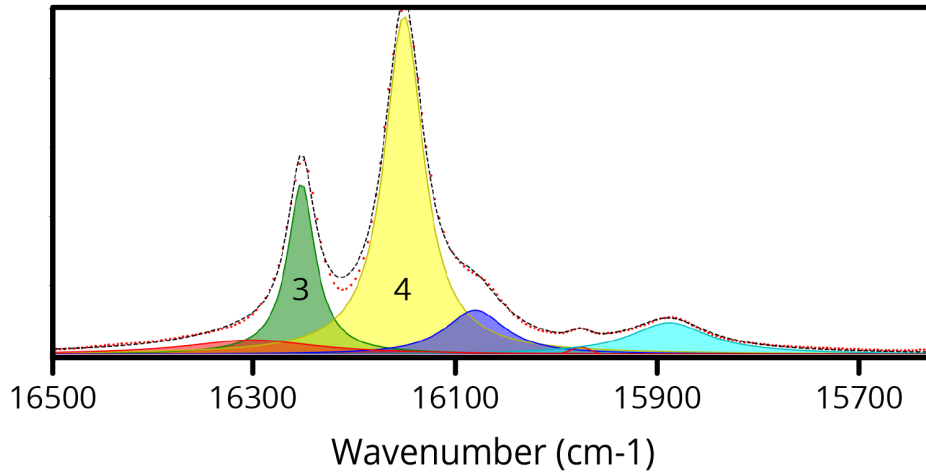


Figure 29. Peak deconvolution of the 5D_0 peaks using the python script

All data was baseline corrected with a linear baseline, which is equal to the mean of the counts in the range $17550 - 17800 \text{ cm}^{-1}$. Finally, all spectra were normalized (to 100) to the biggest peak at 16150 cm^{-1} . This is important to be able to compare spectra as the counts are reliant on the particle density, distance of the probe and temperature and thus varies between measurements.

S3. Oven variance

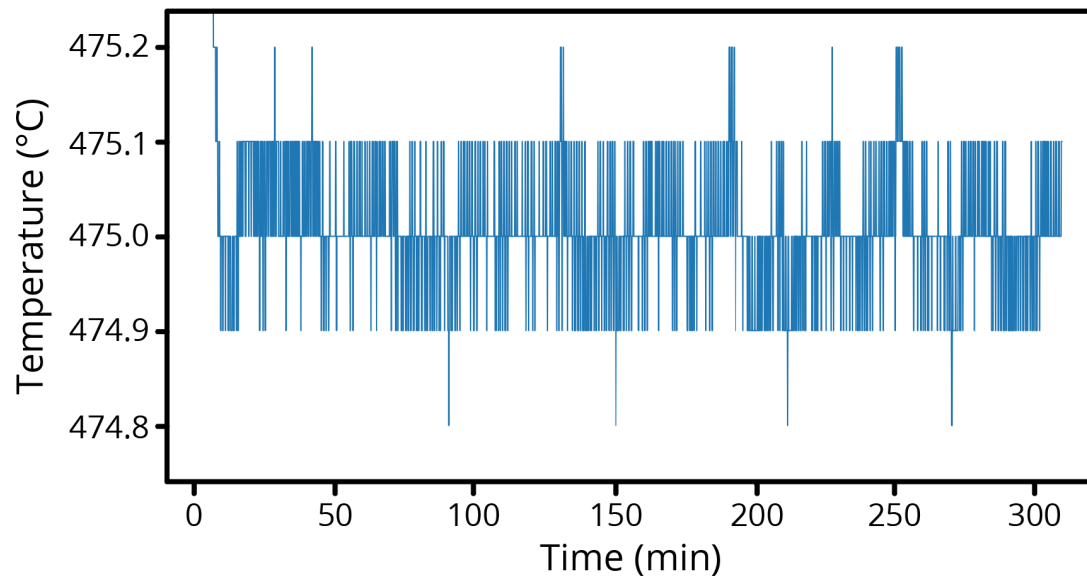


Figure 30. Oven variance in an empty oven with set point $475 \text{ }^\circ\text{C}$

S4. Python script

```
import numpy as np
import scipy as scipy
from scipy import optimize
import pandas as pd
import os
from scipy.optimize import curve_fit
from scipy.optimize import differential_evolution
import warnings
from scipy import integrate
from functools import reduce
import matplotlib.pyplot as plt
import matplotlib.ticker as ticker
from cycler import cycler

""""Section 1 - Formulas""""
pd.set_option('display.max_columns', None)

def Load_Data(File_Path, File_Name, Data_Type, skiprows):
    Data_Type = Data_Type
    if Data_Type == "csv":
        Type_Extension = '.txt'
        Path_Name = str(File_Path) + "/" + str(File_Name) + Type_Extension
        df = pd.read_csv(Path_Name, sep=";", skiprows=skiprows)
    elif Data_Type == "dat":
        Type_Extension = '.dat'
        Path_Name = str(File_Path) + "/" + str(File_Name) + Type_Extension
        df = pd.read_table(Path_Name, sep="\s", skiprows=skiprows)
    elif Data_Type == "excel":
        Type_Extension = '.xlsx'
        Path_Name = str(File_Path) + "/" + str(File_Name) + Type_Extension
        df = pd.read_excel(Path_Name, sep=";", skiprows=skiprows)

    df = pd.DataFrame(df)
    df = df.reset_index(drop=True)
    return df

def Rename_Columns(Data_Frame, Nr_df, Non_Scan_Columns):
    df = Data_Frame
    scans = len(Data_Frame.columns) - Non_Scan_Columns
    df_ColumnNames = ["Wavenumber (cm-1)", 'Dark' + str(Nr_df), 'drop' + str(Nr_df)]
    for i in range(1, scans):
        df_ColumnNames.append("Scan " + str(Nr_df) + '.' + str(i))

    df.columns = df_ColumnNames
    df = df.astype(float)
    df["Wavenumber (cm-1)"] = 1 / (df["Wavenumber (cm-1)"] * 10 ** -7)
    df = df.drop(['drop' + str(Nr_df)], axis=1)
    return df

def give_index(a):
    df_idx = df
    a = df_idx["Wavenumber (cm-1)"].sub(a).abs().idxmin()
    return a

def baseline_correction(Data_Frame, Higher Baseline, Lower Baseline, mean or min):
```

```

df = Data_Frame
dfbase = df.iloc[give_index(Higher_Baseline):give_index(Lower_Baseline):, :]

if mean_or_min == "mean":
    mean = dfbase[sample].mean()
    df[sample] = df[sample] - mean
elif mean_or_min == "min":
    min = dfbase[sample].min()
    df[sample] = df[sample] - min
return df

def normalization(Data_Frame):
    df = Data_Frame
    df[sample] = (df[sample] / df[sample].max()) * 100
    return df

def subtract_reference(Data_Frame, Reference_Frame):
    df = Data_Frame
    dfref = Reference_Frame

    intref =
    integrate.simps(y=dfref.iloc[give_index(Reference_Peak_Upper):give_index(Reference_Peak_Lower), 2])
    int = integrate.simps(y=df.iloc[give_index(Reference_Peak_Upper):give_index(Reference_Peak_Lower), (1 -
    len(Dropped_scans) + i)])

    ratio = intref / int
    df[sample] = df[sample] - (dfref["Scan 1"] / ratio)
    return df

def correction_energy_conversion(Data_Frame):
    df = Data_Frame
    df[sample] = df[sample] / (df["Wavenumber (cm-1)"] ** 2)
    return df

def Plot_Graph_D0(xPlot, yPlot):
    plt.ion()
    f = plt.figure(dpi=100)
    axes = f.add_subplot(111)
    colors = plt.cm.gist_rainbow(np.linspace(0, 1, len(x_peak)))
    plt.gca().set_prop_cycle(cycler('color', colors))

    axes.set_xlim(Higher_Deconvolution, Lower_Deconvolution)
    axes.set_xlabel("Wavenumber (cm-1)", family="serif", fontsize=24)
    axes.set_ylabel("Intensity", family="serif", fontsize=24)

    for peak in range(3, 9): # 0,4
        peak_fit = globals()['voigt_peak_' + str(peak)]
        axes.plot(xData_Peak_Fit, peak_fit)
        axes.fill_between(xData_Peak_Fit, 0, peak_fit, alpha=0.5)

    axes.plot(xData_Peak_Fit, Lorentzian_Fit(xData_Peak_Fit, *copy_Lorentzian_Fit))
    axes.scatter(xPlot, yPlot, s=1)

    mng = plt.get_current_fig_manager()
    mng.full_screen_toggle()
    plt.draw()

```

```

plt.pause(1)
plt.close(f)

def _Lorentzian(x, cenL, ampL, widL):
    return ampL*widL**2/((x-cenL)**2+widL**2)

def _Lorentzian_Fit2(x, cenL1, ampL1, widL1, cenL2, ampL2, widL2):
    return _Lorentzian(x, cenL1, ampL1, widL1) + \
        _Lorentzian(x, cenL2, ampL2, widL2)

def _Lorentzian_Fit(x, cenL3, ampL3, widL3, cenL4, ampL4, widL4, cenL5, ampL5, widL5, cenL6, ampL6,
widL6, cenL7, ampL7, widL7, cenL8, ampL8, widL8):
    return _Lorentzian(x, cenL3, ampL3, widL3) + \
        _Lorentzian(x, cenL4, ampL4, widL4) + \
        _Lorentzian(x, cenL5, ampL5, widL5) + \
        _Lorentzian(x, cenL6, ampL6, widL6) + \
        _Lorentzian(x, cenL7, ampL7, widL7) + \
        _Lorentzian(x, cenL8, ampL8, widL8)

""" Section 2 - Load Data """
# Name the new map. (File_Name) Load the data with ((File path, File name, Data type, number of rows to
drop), Position in the merged data frame, Nr. of columns that dont belong to scans).
File_Name = "3-3-2021"
Input_folder = r"U:/My Documents/Desktop/Master thesis\Data Tjom\EuOCl S7\Raman\raw\3-3-2021 oxy
steps"
dfref = Rename_Columns(Load_Data(r"U:/My Documents/Desktop/Master thesis\Data Tjom\empty oven",
"475C 500ms 30 avg_1810037U1", "csv", 9), 1, 2)
df1 = Rename_Columns(Load_Data(Input_folder, 'experiment 1810037U1', "csv", 9), 1, 2)
#df2 = Rename_Columns(Load_Data(Input_folder, 'Oxy conc 848 - 16816.2_1810037U1', "csv", 9), 2, 2)
#df3 = Rename_Columns(Load_Data(Input_folder, 'Ramp 03 (430-500)_1810037U1', "csv", 9), 3, 2)

# Merge the seperate data frames into one dataframe and correct reference header
Reference_ColumnNames = ["Wavenumber (cm-1)", 'Dark1']
for i in range(1, len(dfref.columns) - 1):
    Reference_ColumnNames.append("Scan " + str(i))
dfref.columns = Reference_ColumnNames

Data_Frames = [df1] # Add an extra data frame if more files are combined
df_merged = reduce(lambda left, right: pd.merge(left, right, on=["Wavenumber (cm-1)"]), Data_Frames)

df_merged = df_merged[["Wavenumber (cm-1)", 'Dark1'] + [c for c in df_merged if c not in ["Wavenumber
(cm-1)", 'Dark1']]] # Add the extra dark here

Total_scans = len(df_merged.columns) - (len(Data_Frames))
merged_ColumnNames = ["Wavenumber (cm-1)", 'Dark1'] # Add the extra dark here
for i in range(1, Total_scans):
    merged_ColumnNames.append("Scan " + str(i))
df_merged.columns = merged_ColumnNames
df = df_merged.astype(float)

Total_scans = (len(df.columns) - (len(Data_Frames) + 1))

""" Section 3 - Correct data: baseline, normalize, dark """
Show_D0 = False # If set to True a plot with peak fit will be shown for all measurements

Measurement = 'Experiment'

```

```

Integration_Averages = 1

skip_measurements = 0 # Choose whether or not you want to skip measurements

Higher_Baseline = 17800 # Insert
Lower_Baseline = 17550 # Insert
Baseline_Type = 'mean' # Choose between mean or min of the baseline range. Insert between '!'

Reference_Peak_Lower = 14680 # If a reference is subtracted enter the range of the peak or area for which
python needs to determine how many times the reference is subtracted
Reference_Peak_Upper = 14950

start_Temp = 0 + skip_measurements # Choose a start Temperature when the x-axis should be a temperature
(Calibration) and 0 for Time (Experiment)

end_Temp = start_Temp + Total_scans - skip_measurements

xData = list(range(start_Temp, end_Temp)) # Is used for a temperature or measurement x-axis
xTime = [] # Is used for a time x-axis

#for i in xData:
#   if i <= len(df1.columns):
#       xTime.append((i * 0.25))
#   else:
#       xTime.append((i * 0.5) - 132.25)

for i in xData: # Insert formula here to convert the xData to time (based on time per measurement)
    xTime.append((i * 0.5))

Dropped_scans = [] # Is needed to correct the lists so the x and y axis stay in sinc
Poisson_Distribution = []

dfref['Scan 1'] = dfref['Scan 1'] - dfref.iloc[:, 1]

for i in range(1 + skip_measurements, Total_scans + 1):
    sample = 'Scan ' + str(i)
    if i <= len(df1.columns) - 2:
        Dark = 1
    elif (len(df1.columns) - 2) < i <= len(df1.columns) + len(df2.columns) - 3:
        Dark = 2
    else:
        Dark = 3

    if df[sample].max() > 60000 or df[sample].max() < 30000: # Can be changed to filter out measurements
with too much or too little signal
        df = df.drop([sample], axis=1)
        del xTime[i-(1 + len(Dropped_scans) + skip_measurements)]
        Dropped_scans.append(sample)
    else:
        df[sample] = df[sample] - df.iloc[:, Dark]

        # df[sample] = df[sample] - dfref['Scan 1'] # if sample needs to be corrected for a constant
reference sample
        # df = subtract_reference(df, dfref) # if sample needs to be corrected by a reference sample
that changes linearly between measurements

    Poisson_Distribution.append(df[sample].max()/100)
    df = correction_energy_conversion(df)
    df = normalization(baseline_correction(df, Higher_Baseline, Lower_Baseline, Baseline_Type))

```

```

print(Dropped_scans)

os.chdir(Input_folder)
File_Name2 = File_Name + ' converted data'
df.to_excel(File_Name2 + '.xlsx', index=False)

""" Section 4 - Calculate integrals for the 5D1 peaks based on the assigned peak ranges """
Int_peak1 = []
Int_peak2 = []

lower_peak1 = 18100
higher_peak1 = 17993
lower_peak2 = 17993
higher_peak2 = 17930

count = 1 + skip_measurements
while count <= Total_scans - len(Dropped_scans):
    for n in range(1, 3):
        a = globals()["lower_peak" + str(n)]
        b = globals()["higher_peak" + str(n)]
        c = globals()["Int_peak" + str(n)]
        Int = integrate.simps(y=df.iloc[give_index(a):give_index(b), count + len(Data_Frames)])
        c.append(Int)

    count += 1

""" Section 5 - Deconvolute 5D0 peaks (Lorentzian peaks) and calculate peak integrals """
x_peak = [16244, 16152, 16080, 15976, 15889, 16250] # Insert guesses for the peaks used for the
deconvolution if more or less peaks are added: add or remove variabls in _Lorentzian_Fit

Lower_Deconvolution = 15650
Higher_Deconvolution = 16550

xData_Peak_Fit = list(range(Lower_Deconvolution, Higher_Deconvolution, 1))

Int_peak3 = []
Int_peak4 = []
Int_peak5 = []
Int_peak6 = []
Int_peak7 = []
Int_peak8 = []

Lower_Bound = []
Upper_Bound = []
y_error = []

assignment = False

correction = 0
dummy = 1 + skip_measurements
while dummy <= Total_scans:
    df_label = "Scan " + str(dummy)

    while True:
        try:
            while True:
                try:
                    df2 = df.iloc[give_index(Higher_Deconvolution):give_index(Lower_Deconvolution), :]
                    xdat2 = df2["Wavenumber (cm-1)"]

```

```

xdat2 = xdat2.values.tolist()
ydat2 = df2[df_label]
ydat2 = ydat2.values.tolist()

if assignment == False:
    a = 3
    for x in x_peak:
        prefix = "L" + str(a)
        df2 = df.iloc[give_index(x + 50):give_index(x - 50), dummy + (len(Data_Frames))]
        A = df2.max() - 5
        globals()["cen" + str(prefix)] = int(x)
        globals()["wid" + str(prefix)] = 10
        globals()["amp" + str(prefix)] = A if A > 0 else 0.1
        Lower_Bound.extend([(x-50), 0, 0]) # Add lower bounds for [peak center, peak width,
peak amplitude]
        Upper_Bound.extend([(x+50), 100, 100]) # Add upper bounds for [peak center, peak width,
peak amplitude]
        a += 1
    assignment = True

ParameterBounds = [Lower_Bound, Upper_Bound]

# Change p0 if peaks were added or removed
popt Lorentzian Fit, pcov Lorentzian Fit = scipy.optimize.curve_fit(Lorentzian Fit, xdat2,
ydat2, p0=[cenL3, ampL3, widL3, cenL4, ampL4, widL4, cenL5, ampL5, widL5, cenL6, ampL6, widL6,
cenL7, ampL7, widL7, cenL8, ampL8, widL8], bounds=ParameterBounds)
perr Lorentzian Fit = np.sqrt(np.diag(pcov Lorentzian Fit))
copy_Lorentzian Fit = popt_Lorentzian Fit

for i in range(3, 3 + len(x_peak)):
    # create separate list for the cen, amp, wid for each peak called: pars ..
    globals()["pars_" + str(i)] = popt_Lorentzian Fit[0:3]
    popt_Lorentzian Fit = np.delete(popt_Lorentzian Fit, [0, 1, 2], axis=0)

    globals()["error_" + str(i)] = perr_Lorentzian Fit[0:3]
    perr_Lorentzian Fit = np.delete(perr_Lorentzian Fit, [0, 1, 2], axis=0)

    # calculate the Lorentzian peaks based on the cen, amp and wid for each peak
    a = globals()["pars_" + str(i)]
    globals()["voigt_peak_" + str(i)] = Lorentzian(xData_Peak Fit, *a)

    # calculate the area for the separate peaks
    globals()["area_" + str(i)] = np.trapz(globals()["voigt_peak_" + str(i)])

    # add the peak integrals to the separate list for each peak
    peak_integral = globals()["Int_peak" + str(i)]
    peak_integral.append(globals()["area_" + str(i)])

    # make the result the new guess to reduce calculation times
    globals()["cenL" + str(i)] = a[0]
    globals()["ampL" + str(i)] = a[1]
    globals()["widL" + str(i)] = a[2]

    if globals()["ampL" + str(i)] or globals()["widL" + str(i)] == 100 or 0:
        globals()["ampL" + str(i)] = 80
        globals()["widL" + str(i)] = 10

if Show_D0 == True:
    Plot_Graph_D0(xdat2, ydat2)

```

```

A = Int_peak1[correction - 1] + Int_peak2[correction - 1]
# Add or remove pars ...[1] and [2] if peaks were added or removed
peak_sum = pars_3[2] * pars_3[1] + pars_4[2] * pars_4[1] + pars_5[2] * pars_5[1] + pars_6[2] *
pars_6[1] + pars_7[2] * pars_7[1] + pars_8[2] * pars_8[1]

sum_error = 0.0

for i in range(3, 3 + len(x_peak)):
    fit_error = (((globals()['pars_' + str(i)])[2] * A)/(np.pi * 2 * peak_sum))**2 * (globals()['error_' +
str(i)][2])**2 + (((globals()['pars_' + str(i)])[1] * A)/(np.pi * 2 * peak_sum))**2 * (globals()['error_' +
str(i)][1])**2)
    sum_error = sum_error + fit_error

sum_error = np.sqrt(sum_error)
y_error.append(sum_error)
print(sum_error)

correction += 1
print('status: ' + str(dummy))
break
except RuntimeError:
    assignment = False

del xTime[correction]
del Int_peak1[correction]
del Int_peak2[correction]
print(dummy)
break
break
except KeyError:
    break
dummy += 1

""" Section 6 - Convert integrals to a dataframe, define peaks for peak ratio and prepare results. """
# Change integral column_stack and .columns if peaks were added or removed
integral = np.column_stack((xTime, Int_peak1, Int_peak2, Int_peak3, Int_peak4, Int_peak5, Int_peak6,
Int_peak7, Int_peak8, y_error, Poisson_Distribution))
integral = pd.DataFrame(integral)

def Temp(E, y, R):
    return (-E/(0.695 * np.log(y/R)))-273

deltaE = 1841 # Enter the found values from the Boltzmann Fit to convert peak ratio to Temperature
R = 0.083

integral.columns = ['Time', 'peak1', 'peak2', 'peak3', 'peak4', 'peak5', 'peak6', 'peak7', 'peak8', 'y_error',
'Poisson Error']
integral['5D0_ratio'] = integral.apply(lambda x: (x.peak4 / x.peak3), axis=1)
integral['5D1_ratio'] = integral.apply(lambda x: (x.peak1 / x.peak2), axis=1)
integral['peak_ratio'] = integral.apply(lambda x: (x.peak1 + x.peak2) / (x.peak3 + x.peak4), axis=1) # Define
the peak ratio you want to calculate here
integral['y_error'] = integral.apply(lambda x: x.peak_ratio * x.y_error, axis=1)
integral['Temp'] = integral.apply(lambda x: (Temp(deltaE, x.peak_ratio, R)), axis=1)
integral['peak_12'] = integral.apply(lambda x: ((x.peak1 + x.peak2) * x.Poisson_Error), axis=1)
integral['peak_34'] = integral.apply(lambda x: ((x.peak3 + x.peak4) * x.Poisson_Error), axis=1)
integral['Poisson error'] = integral.apply(lambda x: (((0.695 * x.Temp**2/ deltaE) * (np.sqrt((1/x.peak_12) +
(1/x.peak_34)))) / np.sqrt(Integration_Averages), axis=1)

integral.to_excel('Int ' + File_Name + '.xlsx', index=False)

```

```

D0_ratio = integral['5D0_ratio']
D1_ratio = integral['5D1_ratio']
peak_ratio = integral['peak_ratio']
Time = integral['Time']/60
y_error = integral['y_error']
Temperature = integral['Temp']
Poisson_Error = integral['Poisson error']

""" Data analysis of an experiment """
if Measurement == 'Experiment':

    fig, ax = plt.subplots()
    ax.scatter(Time, Temperature, color="red", marker="o", s=5, label="Intensity ratio")
    ax.errorbar(Time, Temperature, yerr=Poisson_Error, fmt='none', ecolor='black', elinewidth=1, capsize=3,
errorevery=5)
    ax.set_xlabel('Time (hours)', family="serif", fontsize=20)
    ax.set_ylabel('Temperature', family="serif", fontsize=20)
    ax.xaxis.set_major_locator(ticker.MultipleLocator(1.0))
    ax.xaxis.set_minor_locator(ticker.MultipleLocator(0.5))
    plt.yticks(fontsize=16)
    plt.xticks(fontsize=16)

    ax2 = ax.twinx()
    ax2.set_ylim([2.0, 2.5])
    ax2.plot(Time, D0_ratio, color='blue', label="D0 intra level peak ratio")
    ax2.plot(Time, D1_ratio, color="green", label="D1 intra level peak ratio")
    plt.yticks(fontsize=16)

    plt.show()

""" Data analysis for a calibration - Boltzmann Fit """
if Measurement == 'Calibration':
    yData = peak_ratio
    xData = Time

    def func(x, a, b):
        return a * np.exp(-b/(0.695*(x+273)))

    # function for genetic algorithm to minimize (sum of squared error)
    def sumOfSquaredError(parameterTuple):
        warnings.filterwarnings("ignore") # do not print warnings by genetic algorithm
        val = func(xData, *parameterTuple)
        return np.sum((yData - val) ** 2.0)

    def generate_Initial_Parameters():
        # min and max used for bounds
        maxX = max(xData)
        minX = min(xData)

        parameterBounds = []
        parameterBounds.append([minX, maxX]) # search bounds for a
        parameterBounds.append([minX, maxX]) # search bounds for b

        # "seed" the numpy random number generator for repeatable results
        result = differential_evolution(sumOfSquaredError, parameterBounds, seed=3)
        return result.x

# generate initial parameter values

```

```

geneticParameters = generate_Initial_Parameters()
print(geneticParameters)
# curve fit the test data
fittedParameters, pcov = curve_fit(func, xData, yData, geneticParameters, maxfev=10000)

print('Parameters: \nR0: ', fittedParameters[0], '\ndelta E: ', fittedParameters[1])

modelPredictions = func(xData, *fittedParameters)
absError = modelPredictions - yData

SE = np.square(absError) # squared errors
MSE = np.mean(SE) # mean squared errors
RMSE = np.sqrt(MSE) # Root Mean Squared Error, RMSE
Rsquared = 1.0 - (np.var(absError) / np.var(yData))
print('Dropped scans: ' + str(Dropped_scans))
print('RMSE:', RMSE)
print('R-squared:', Rsquared)

# Make-up statistics for Boltzmann figure
text = str('R0: ') + str(round(fittedParameters[0],3)) + str('\ndelta E: ') + str(round(fittedParameters[1],0)) +
str('\nRsquared: ') + str(round(Rsquared,4))

# graphics output section
def ModelAndScatterPlot(graphWidth, graphHeight):
    f = plt.figure(figsize=(graphWidth / 100.0, graphHeight / 100.0), dpi=100)
    axes = f.add_subplot(111)

    # first the raw data as a scatter plot
    axes.plot(xData, yData, '.r', markersize= 2)
    # create data for the fitted equation plot
    xModel = np.linspace(min(xData), max(xData))
    yModel = func(xModel, *fittedParameters)

    # now the model as a line plot
    axes.plot(xModel, yModel, linewidth=1, color='black')

    axes.set_xlabel('Temperature') # X axis data label
    axes.set_ylabel('5D1/5D0 peak ratio') # Y axis data label

    plt.figtext(.15, .75, text)
    plt.title('Boltzmann fit', fontsize=26)
    plt.show()
    plt.close('all') # clean up after using pyplot

graphWidth = 800
graphHeight = 600
ModelAndScatterPlot(graphWidth, graphHeight)

```